JOURNAL OF GEOPHYSICAL RESEARCH, VOL. 100, NO. C2, PAGES 2591–2611, FEBRUARY 15, 1995

X band microwave backscattering from ocean waves

P. H. Y. Lee, J. D. Barter, K. L. Beach, C. L. Hindman, B. M. Lake,
H. Rungaldier, J. C. Shelton, A. B. Williams, R. Yee, and H. C. Yuen
TRW Space and Electronics, Redondo Beach, California

Abstract. Backscattering experiments at microwave frequencies were conducted off the west coast of Scotland in the summer of 1991. Using a dual-polarization, eight-frequency, X band, coherent scatterometer mounted on the bow of a boat, we measured time-resolved backscattering from ocean waves at a range of grazing angles from 10° to 70°. From the grazing-angle-dependent signals and their Doppler spectra, we are able to differentiate Bragg scattering from non-Bragg scattering and resolve "peak separation" between the vertical and horizontal polarizations. We observe instances of "super" events, i.e., instances when the horizontal polarization return power equals or exceeds the vertical polarization power at particular frequencies. We find that "super" events occur not only at low grazing angles but at any grazing angle for upwind viewing directions and obtain statistics for such occurrences as a function of grazing angle. We study the coherence properties of scatterers and find strong evidence that at low grazing angles, lifetime-dominated, non-Bragg scattering contributes noticeably to returns of both polarizations, but is dominant in providing returns for the horizontal polarization. We examine "spiking" events and find that they can be related to, but need not be limited to, breaking wave events. By comparing the data of upwind runs with cross-wind and circle runs, we obtain wind direction dependence of Doppler spectra, which further assists in the identification of scattering mechanisms.

1. Introduction

During the month of July 1991 we participated in a series of experiments at Loch Linnhe and the Sound of Sleat in western Scotland. During that time we conducted microwave backscattering experiments from wind wave surfaces for different wind conditions at a variety of grazing angles. The objective of our experiment was to obtain a database to facilitate the evaluation of hydrodynamic-electromagnetic interaction models in order to gain a better understanding of the physics of backscattering of microwaves from ocean surfaces in general, and of low-grazing-angle (LGA) backscattering in particular. Historically, experiments on LGA backscattering have provided the microwave scattering community with some rather peculiar results [*Goldstein*, 1947; *Pidgeon*, 1968; *Mel'nichuk and Chernikov*, 1971; *Long*, 1974; *Leykin et al.*, 1975; *Kalmykov and Pustovoytenko*, 1976]. These results have challenged theoreticians for some time, and in spite of rather intense study in past and recent years, the problems of LGA scattering have proven to be remarkably resistant to analytical solution. In order to correctly model the problem, the underlying physics must first be thoroughly understood. Our approach is therefore to conduct experiments which we hope will identify the fundamental scattering mechanisms.

2. The Microwave Scatterometer

Our principal instrument for microwave measurements is a CW, dual-polarization, X band, coherent scatterometer, designed to operate at four nominal frequency pairs as shown in Table 1. The close frequency spacing between polarization channels in a pair facilitates polarization ratio measurement, while the wide spacing between pairs provides rapid speckle averaging. In order to avoid interference from X band equipment used by other participants in the Scotland experiment, the actual frequencies used in the field differed slightly from the nominal values.

A block diagram of the X band scatterometer is shown in Figure 1. The two 25-cm-diameter corrugated horns, separated by 28 cm (center to center), have a "toe-in" angle of 1.09°. The total transmitted power of the scatterometer is 1 W. The receiver preamplifier noise figure is 2.1 dB. Microwave relays are used to switch the radar from an operating configuration to an internal calibration configuration where the transmitter and receiver are connected to each other via a 60-dB attenuator or to a null configuration where both transmitter and receiver are connected to resistive terminations. An additional set of relays are provided which can reconfigure the radar to measure cross-polarized scattering (VH, HV); however, only the copolarized (HH, VV) capability was used in the 1991 experiment. Programmable attenuators are provided between the receiver horn and the low-noise amplifier of each polarization. These attenuators were set for each grazing angle and sea state to keep the recorded signal on scale. The complete scatterometer system, contained in a waterproof metal box, was mounted on an extended platform on the starboard side of the bow of the 80-ton, 24-m-long research vessel *Loch Nevis*. The scatterometer could be rotated about a hinge (located at the bottom of the box, 2.275 m above the mean water surface) which allowed the grazing angle to be varied.

The scattered signals of each polarization are detected by

Paper number 94JC02741.
0148-0227/95/94JC-02741$05.00

Table 1. Frequency Pairs for Microwave Scatterometer

	Polarization, GHz	
Pair	Vertical	Horizontal
1	9.020	9.021
2	9.170	9.171
3	9.320	9.321
4	9.470	9.471

four quadrature mixers, one for each transmitted frequency. Each mixer generates an in-phase (I) and quadrature (Q) signal with a frequency response of 0 to 1000 Hz. With complex amplitude thus generated for each frequency, there are 16 channels of output. During an experiment the 16 signals are recorded digitally on a multichannel cassette recorder.

An absolute calibration of the scatterometer system [*Barter et al.*, 1993] was conducted in a large (10 m × 10 m × 30 m) anechoic chamber using spheres and cylinders of various sizes as well as corner reflector targets. Measurements consisted of establishing the output power and receiver gain of each of the eight frequency channels, the system radiation patterns in two perpendicular planes in the forward half sphere, the range dependence of the signal power, and the cross-polarization isolation of the scatterometer system. The essential results of the calibration are as follows: total power (eight channels), ~1 W; nominal receiver gain each channel, ~60 dB; system radiation pattern, approximately Gaussian main lobe; azimuthal plane −3 dB beam width, 8.7° for VV and 10.3° for HH; vertical plane −3 dB beam width, 11° for VV and 9.6° for HH; average −3 dB beam width, 9.5°; antenna gain, 26.6 dB; cross-polarization isolation, >35 dB; image rejection ratio, ~−45 dB.

As an example, the measured two-way antenna pattern in the azimuthal plane (the plane containing the scatterometer boresight and the line connecting the centers of both horns) is shown in Figure 2. Note the relatively good symmetry between HH and VV patterns. Also note that the two-way sidelobes are small (<−65 dB).

In addition to the microwave scatterometer used for the present experiment, we also fielded a surface truth sensor package which contained a scanning laser slope gauge [*Lee et al.*, 1992], which measures slopes of waves in the 1- to 10-cm range; capacitance wire wave height gauges, which measure wave amplitudes of waves longer than 10 cm; and other diagnostics which measured meteorological conditions, sea state, bulk water parameters, and ship velocity [*Barter et al.*, 1991].

A scaled model of the instrument platform *Loch Nevis* was tested in a wind tunnel with a cross section 0.89 m high by 1.22 m wide [*Barter et al.*, 1992a]. A model scale of 1:79 was chosen to yield a model length of approximately one-quarter the tunnel width and a model height of approximately one-seventh the tunnel height. Wind speeds were chosen so that the friction velocities in the boundary layer of the wind tunnel matched the friction velocities obtained in the field experiment. The wind fields at different positions on the scaled model and at different angles of free stream wind direction with respect to boat heading were thus mapped out. This allowed the appropriate wind field corrections (if any) to be taken into account for data reduction purposes. Also, the results of our scaled model wind tunnel measurements have been shown to be in very good agreement with all testable environmental observations obtained during the field experiment.

3. Experiments and Data Processing

Once per day during field experiments, an internal calibration sequence of the scatterometer was recorded on tape. This sequence consisted of 10 s each of the calibration configuration and the null configuration, while stepping the V and H input attenuators through their 0- to 70-dB span. Also, a one-time radiometric field calibration was performed using a small test sphere as a moving target.

The scatterometer data from actual ocean backscattering

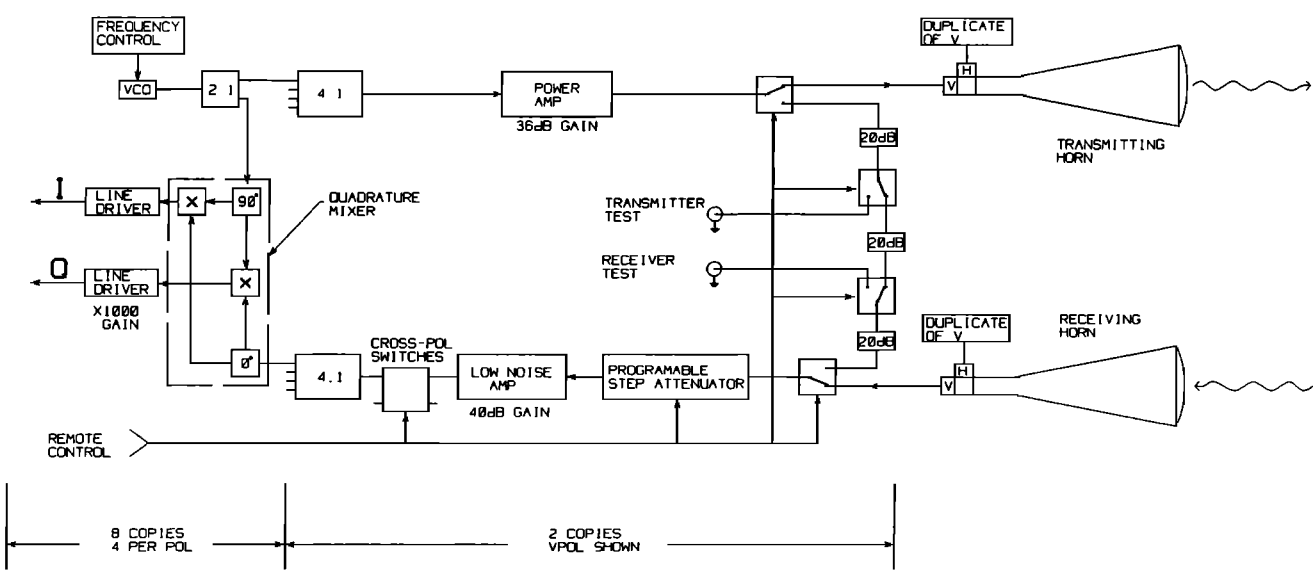

Figure 1. A schematic diagram of the dual-polarized, eight-channel, X band, coherent scatterometer.

runs were recorded at a sampling rate of 5 kHz and downsampled by strict averaging of each input channel to 1.25 kHz to conserve data archive volume. Preliminary data reduction included high-pass filtering to eliminate DC offsets and static returns, and low-pass filtering with decimation to restrict the Doppler range to ±3.25 m/s. Final data reduction techniques were tailored to each of the various results. We will present speckle-averaged, time-resolved return losses, and time-resolved as well as time-averaged return loss spectral densities (Doppler spectra) for both HH and VV polarizations. Return loss refers to the ratio of the received signal to the transmitted signal and is thus specific to the scatterometer system. Its absolute measurement depends on the calibration data. The absolute radar cross section per unit area of scattering surface is obtained from the return loss using the measured antenna pattern mentioned in the previous section.

An estimate of the effects of statistical fluctuations on the ensemble-averaged spectral densities, $G_{xx}(f)$, may be obtained [*Bendat and Piersol*, 1986] from the number of disjoint spectra in an ensemble (n_d) and the frequency resolution of the spectra (B_e). B_e and n_d are related by $n_d = B_e T_R$, where T_R is the total record length. The degrees of freedom for a spectral estimate is given by $n = 2n_d$. For the power spectral densities (PSDs) presented in this paper (except for the time-resolved spectra and circle run spectra, which have shorter T_R), $B_e = 2.44$ Hz and $n_d = 300$, which give a normalized random error for the estimated spectra of $\varepsilon_r = n_d^{-1/2} = 0.058$, or an error bar of (+0.26, −0.24) dB/Hz. The corresponding bias error is small. In the worst case it is $\varepsilon_b = (B_e^2/24)[G''_{xx}(f)/G_{xx}(f)] = 0.025$, which corresponds to an error bar of ±0.11 dB/Hz. For Royal Signals and Radar Establishment (RSRE) pulsed radar data (the RSRE data at grazing angle $\theta_g = 6°$ were obtained in 1989 at Loch Linnhe, Scotland; data kindly provided by K. Ward (Defence Research Agency, Malvern, U.K., private communication, 1993)), $B_e = 0.98$ Hz and $n_d = 50$, giving $\varepsilon_r = 0.14$ and $\varepsilon_b = 4.0 \times 10^{-3}$, or corresponding error bars of (+0.66, −0.57) dB/Hz and ±0.017 dB/Hz, for random error and bias error, respectively.

The scattering-object velocity in the water frame of reference (i.e., horizontal reference frame) is obtained from the measured Doppler frequency given by

$$f_D = \frac{2 \cos \theta_g}{\lambda} (v_b \pm v_w \pm v_c \pm c_p), \tag{1}$$

where θ_g is the scatterometer local grazing angle, λ is the microwave free space wavelength, and v_b, v_w, v_c, and c_p refer to boat speed, wind drift, current velocity (including the effect of orbital motion [*Lee*, 1977]), and the speed of the scattering object on the water surface, respectively. Note that (1) is approximate, since the surface tilt and vertical motion are ignored. The plus and minus signs refer to contributions from approaching or receding scatterers, respectively. If the speed of the scattering object is associated with the underlying water wave, then c_p is the phase speed of the water wave given by

$$c_p = \left(\frac{g}{k_w} + \frac{\gamma}{\rho} k_w\right)^{1/2}, \tag{2}$$

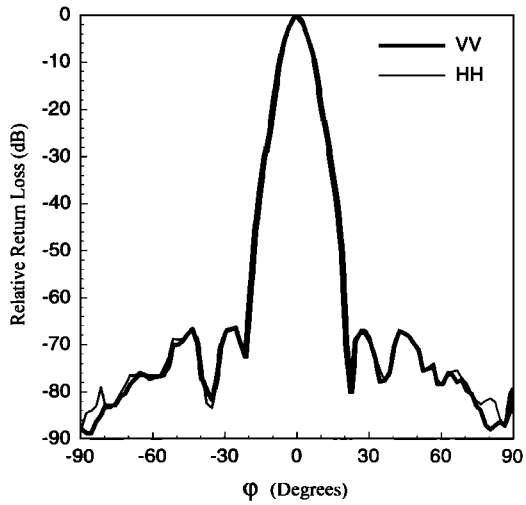

Figure 2. The calibrated two-way radiation pattern in the azimuthal plane.

where g is the gravitational acceleration, γ and ρ are the water surface tension and density, respectively, and k_w is the associated wavenumber. For Bragg scattering,

$$k_w = k_B \equiv \frac{4\pi \cos \theta_g}{\lambda} \tag{3}$$

is the Bragg-resonant wavenumber in water. Research has shown that a good approximation to the wind drift is 2.6–5.5% of the wind speed [*Lange and Hühnerfuss*, 1978], we use 3% because it provides a slightly better agreement to our data.

The data considered here consist of upwind, cross-wind and circle runs. During the runs, surface truth data were simultaneously collected using the diagnostics described in the surface truth sensor package. Data gathering runs were conducted at boat speeds in the range of 0.9–1.4 m/s. The wind speeds at 10 m above the water surface (U_{10}) were in the range of 5–13.5 m/s for the data presented. The experimental configuration is given in Figure 3, where the angles and velocities of interest for the experiment are depicted for an upwind run configuration. For a downwind run, the velocities U_{10}, v_w and c_p are reversed. For cross-wind runs, the velocities U_{10} and v_w are perpendicular to the paper.

4. Results

4.1. Grazing Angle Dependence of Time-Averaged Doppler Spectra

In what follows, the Doppler spectra are presented as return loss spectral density plotted against Doppler frequency. Based on the definition of return loss mentioned earlier, the return loss spectral density is simply a normalized PSD. The Doppler frequency corresponds to radial velocity with respect to the scatterometer bore sight. The interpretation of the Doppler spectra is made clear by reference to (1), which states that the frequency of any particular feature (e.g., a spectral peak) is simply the sum of the various speeds multiplied by the factor $2 \cos \theta_g/\lambda$. This is depicted in Figure 4. Also indicated in this figure is the spectral image at negative Doppler frequencies (recall that the image rejection ratio is ~−45 dB), which is due to

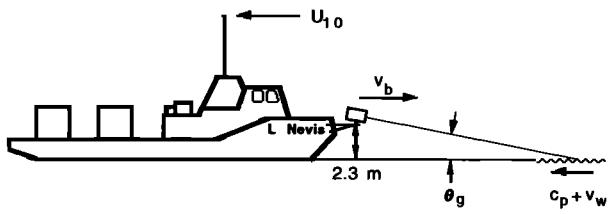

Figure 3. A schematic of the experimental configuration for an upwind run. For a downwind configuration, the direction of U_{10}, v_w, and c_p are reversed. For cross-wind configurations, U_{10} and v_w are perpendicular to the paper.

nonideal quadrature mixers in the scatterometer system. There is also the presence of a low-frequency bump (at frequencies below ~30 Hz) as well as a (sometimes distinct) bump centered at 0 Hz; the former is due to an instrument response to the platform vibration (microphonic artifact), while the latter is due to DC drift. Both are instrumental artifacts which are avoided by the choice of platform velocity; i.e., the boat speed effectively shifts the signals of interest away from the low-frequency artifacts.

4.1.1. Upwind runs. The term upwind run refers to a data-collection run during which the scatterometer is looking against the propagation direction of the dominant wave. The results for upwind runs for grazing angles between 10° and 70° together with the corresponding environmental, computed and geometrical data are given in Table 2. In Table 2, θ_g, U_{10} and v_b are measured values; v_w is taken as 3% of U_{10}; c_p is the Bragg wave phase speed computed from (2) and (3); a and b are the major and minor (radial and azimuthal) half-axes of the elliptical footprint computed from the intersection of a cone and a plane inclined at an angle of θ_g; the cone angle is taken to be the average −3-dB beam width of 9.5°; and f_D is the Doppler frequency, corresponding to scattering from Bragg-resonant waves, computed from (1). The friction velocity u_* is provided for reference. The boat speed is measured relative to large-scale currents (if any), so the effects of circulation currents do not contribute to Doppler frequency shifts in the boat frame of reference. The sea state is characterized by the rms wave height a_{rms} and the gravity wave frequency f_{dom} at the peak of the wave height spectrum. These sea state data were obtained from a Johns Hopkins University Applied Physics Laboratory (JHU/APL) spar buoy located within 1 km of our platform track and were kindly provided by R. Chapman (JHU/APL, Laurel, Maryland, private communication, 1993). Some of the times of measurement were coincidental with our scatterometer data collection time; otherwise, the sea state data corresponding to the identical or closest value of U_{10} were used. From the f_{dom} data in Table 2, we note that very long waves are absent for our experiments. Maximum instrument platform pitch and roll are limited to ±1.25° and ±1.25°, respectively. In the last two columns of Table 2, the frequencies of the "slow" and "fast" PSD peaks (discussed below) observed in the respective Doppler spectra are given. Orbital velocities of dominant waves calculated from data in Table 2 are in the range of 0.07–0.023 m/s. The effect of orbital speed is neglected, since we assume that the positive and negative contributions cancel out, an assumption which is justified by the data.

Examination of the 1-min time-averaged Doppler spectra reveals that at large grazing angles, the HH profile is similar to the VV profile, both peaking at more or less the same frequencies. We notice, in addition to the familiar Bragg resonant peak in the PSD, also a peak at higher frequency. These will be designated as "slow" and "fast" peaks, respectively. We also note that the HH profile is sensitive to the grazing angle. As the grazing angle is decreased, the peak of the HH spectrum gradually shifts toward higher Doppler frequencies, thus causing a separation of the HH peak from the VV peak. A few examples are shown to illustrate this point. In Figure 5 the Doppler spectra for both HH and VV returns are quite similar at large grazing angle (θ_g = 55°) where the slow and fast peaks are identified. As the grazing

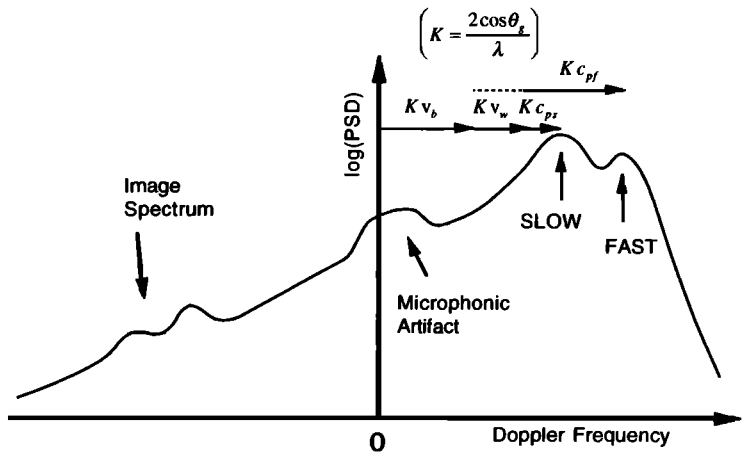

Figure 4. A schematic of a typical Doppler spectrum for an upwind run with Bragg waves and fast scatterers approaching the boat. The contributions of various speeds to the slow and fast peaks are noted. In a downwind run, the wind drift contribution is reversed in direction, while in a cross-wind run, the wind drift contribution drops out. If Bragg waves (or fast scatterers) are receding from the boat, the direction of c_{ps} (or c_{pf}) is reversed. If c_{pf} is very large, then the contribution of wind drift is negligible (indicated by the dashed line under Kc_{pf}). The image spectrum at negative Doppler frequencies, DC drift, and microphonic response are instrumental artifacts.

Table 2. Data Summary of TRW Upwind Runs at Different Grazing Angles θ_g

θ_g, deg	U_{10}, m/s	v_b, m/s	v_w, m/s	c_p, m/s	f_D, Hz	a, m	b, m	u_*, cm/s	a_{rms}, cm	f_{dom}, Hz	f_s, Hz	f_F, Hz
10	8.5	1.15	0.26	0.23	99.4	8.86	1.54	32	5.8	0.45	99	160
15	6.0	0.9	0.18	0.23	78.3	3.43	0.89	21	2.0	0.70	77	140
20	6.0	1.25	0.18	0.23	96.6	1.87	0.64	21	1.8	0.65	105	156
25	9.5	1.10	0.29	0.23	90.7	1.20	0.51	37	3.9	0.55	83	135
30	6.5	1.15	0.19	0.23	84.2	0.85	0.42	23	1.8	0.65	86	160
35	8.0	1.10	0.24	0.23	79.6	0.64	0.37	29	3.9	0.53	85	136
45	5.0	1.25	0.15	0.24	71.8	0.42	0.30	17	1.8	0.65	79	105
55	7.5	1.15	0.23	0.24	57.5	0.31	0.25	27	4.4	0.68	58	89
65	13.5	1.10	0.40	0.27	46.3	0.25	0.23	60	5.7	0.48	59	73
70	11.0	1.15	0.33	0.29	37.5	0.22	0.21	45	5.1	0.48	41	62

Parameters are wind speed at 10-m height, U_{10}; boat speed v_b; calculated wind drift v_w; computed Bragg resonant wave phase speed c_p; and Doppler frequency f_D; the characteristic lengths of the antenna footprint, a and b; the friction velocity u_*; the rms wave amplitude a_{rms} and dominant wave frequency f_{dom} of the ocean wave-amplitude spectrum; and the observed Slow (Bragg) and Fast (faster than Bragg) frequencies f_S and f_F

angle is reduced to $\theta_g = 25°$ (Figure 6), although the "slow" peak is still dominant in the VV return, the "fast" peak is slightly larger (by a few decibels in spectral density) than the slow peak in the HH return, in other words, we have recorded peak shifting (the shift from the slow to the fast peak) in transition. At a grazing angle of $\theta_g = 10°$ (Figure 7), peak separation has occurred. The fast peak has become the dominant peak of the HH Doppler profile, and only several gentle "wrinkles" remain in the profile at the frequency location of the slow peak. Finally, for RSRE pulsed-radar data at $\theta_g = 6°$ shown in Figure 8, we see complete peak separation. The VV and HH spectra shown in Figure 8 are for one typical range cell. The nominal range of the RSRE radar is 2.5 km; the cell resolution is 1.5 m in range and nominally ~43 m in azimuth. The look angle is ~60° with respect to the wind direction, the wind speed is ~8 m/s (i.e., the head wind component is ~4 m/s). Note that the HH profile is completely dominated by the "fast" peak without any hint that a slow component is present. Likewise, the VV profile is completely dominated by the "slow" peak with little indication that a fast component is present. This separation of VV and HH peaks is typical of Doppler spectra seen at very low grazing angles [*Pidgeon*, 1968; *Valenzuela and Laing*, 1970].

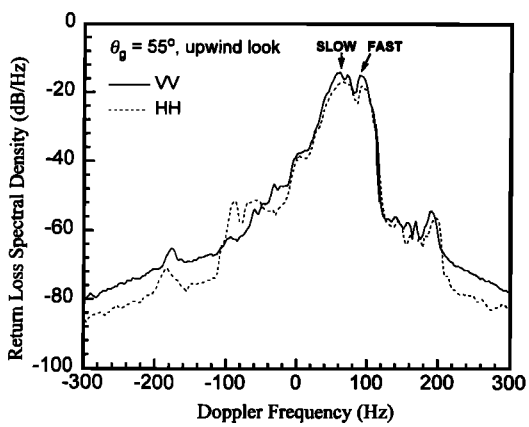

Figure 5. Time-integrated Doppler spectra of wind waves; upwind look direction, $\theta_g = 55°$. The VV trace has higher spectral density at both "slow" and "fast" peaks. The frequencies of the slow and fast peaks are given in Table 2. The slow peak corresponds to contribution from Bragg scatterers, while the speed corresponding to the fast peak can be evaluated from Equation (1) using environmental data given in Table 2. In this particular case, the fast scatterer corresponds to the phase speed of a gravity wave of 0.83 m wavelength.

We see then that peak separation is more accurately understood as a gradual relinquishing of dominance by the slow peak of the HH spectra with decreasing grazing angle. We will refer to the grazing angle at which dominance in the HH spectrum is transferred as the "switch-over" angle. We find that for wind speeds of 5–13.5 m/s, switch-over occurs at grazing angles between 25° to 15°. The switch-over angle is probably wind speed and sea state dependent. Since these data were gathered at sea and not obtained under controlled laboratory conditions, a more precise value of the switch-over grazing angle is not available at this time.

At each grazing angle, the Doppler frequency at the slow peak corresponds reasonably well to that given by (1), with c_p matching the phase speed of the Bragg-resonant water wave. This can be seen in Table 2 and the examples of Doppler spectra shown in Figures 5–7. The fact that $f_s \sim f_D$ (more or less) justifies the assumption that effects of orbital speed cancel out. Stokes drift, being a higher-order term, is neglected. We note from our data that at wind speeds less than ~5 m/s, a smaller Bragg peak at lower frequency corresponding to the receding Bragg waves can also be seen, especially at lower grazing angles where the frequency resolution is favorable (because cos θ_g is near unity); however for the sea state conditions given in Table 2, the individual Bragg peaks cannot be resolved. This "smearing" of Bragg peaks for higher sea states was also observed by *Plant* [1990].

The fast peak, however, corresponds to scatterers which move at speeds much faster than the Bragg wave speed. If one assumes that the fast scatterer is associated with the phase speed of a gravity wave, then the specific values of each case can be evaluated from the f_F data given in Table 2. Specifically, from f_F, (1) is used to compute the phase speed of the fast scatterer, and (2) is used to compute the corresponding gravity wave wavelengths which are given in the captions of Figures 5, 6, and 7. We shall return to this point later.

4.1.2. Cross-wind runs. A cross-wind run means that the scatterometer is looking perpendicular to the propaga-

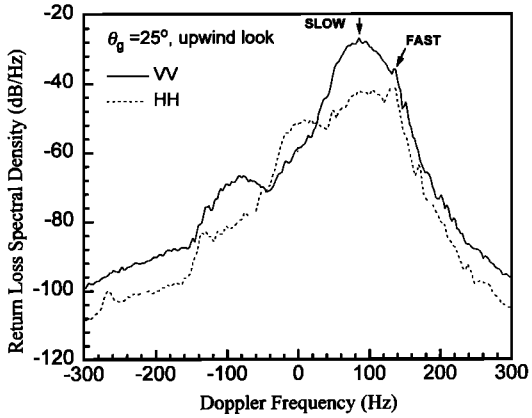

Figure 6. Time-integrated Doppler spectra of wind waves, upwind look direction, θ_g = 25°. The VV trace has higher spectral density at both slow and fast peaks. Peak separation of HH relative to VV is in progress (see text). The fast scatterer corresponds to the phase speed of a gravity wave of 0.68-m wavelength.

tion direction of the dominant wave. While prominent fast peaks are present in the Doppler spectra for upwind runs, their presence is greatly reduced in cross-wind runs at low grazing angles and unnoticeable in the cross-wind runs for all grazing angles greater than ~25°. For cross-wind viewing directions, peak separation does not occur for low grazing angles; i.e., both the VV and HH spectra peak at more or less the same frequency. Three examples are shown in Figure 9, for θ_g = 55°, 25°, and 10°. In this figure, for the cases at 10° and 25°, the bump in the HH spectrum (at frequencies below 30 Hz) is due to instrumental artifacts mentioned earlier (see text describing Figure 4) and should be ignored. At large grazing angles the artifacts are less obvious because their presence is masked by the high-level Bragg signals. Comparison of the cross-wind spectra with Figures 5, 6, and 7 (for upwind spectra) reveals the obvious absence of a prominent fast peak. Although fast scatterers are noticeable in the 10° HH spectrum, the PSD value is smaller than the Bragg peak value. The comparison of upwind and cross-wind results also provides a clear indication that the ocean is not an isotropic scatterer. To first order, the observed Doppler frequency in the cross-wind case corresponds quite well to the boat velocity. Closer scrutiny, however, reveals that the peak may be slightly upshifted or downshifted from the "reference frequency" (i.e., Doppler frequency corresponding to boat speed only) depending on whether approaching or receding Bragg waves, respectively, were dominant in contributing to the backscatter return. If both approaching and receding Bragg wave contributions were equal, then an appropriate broadening of the Doppler spectrum about the "reference frequency" is observed. Specifically, (1) for the θ_g = 55° cross-wind run, U_{10} = 7.5 m/s and the boat speed is 1.15 m/s. If the Bragg peaks due to approaching and receding Bragg waves were resolvable, they would appear at 49 Hz and 32 Hz, respectively. The observed single peak in the spectrum, however, is located near 35 Hz. (2) For the θ_g = 25° cross-wind run, U_{10} = 9.5 m/s and the boat speed is 1.1 m/s. If the Bragg peaks due to approaching and receding Bragg waves were resolvable, they would appear at 74 Hz and 49 Hz, respectively. The observed peak in the spectrum, however, is located at 57 Hz. (3) For the θ_g = 10° cross-wind run, U_{10} = 8.5 m/s and the boat speed is 1.15 m/s. If the Bragg peaks due to approaching and receding Bragg waves were resolvable, they would appear at 83.6 Hz and 55.8 Hz, respectively. The observed peak in the spectrum is located at 67 Hz. Thus we believe that it is the rough sea state that renders the peaks unresolvable. For the most part, cross-wind viewing angles provide results that can be adequately described by Bragg scattering. Because of the drop in the Bragg signals relative to the fast-scatterer signals in the HH spectrum at the low grazing angle of 10°, fast scatterer contributions at greater than 120 Hz are noticeable, but the Bragg signals are still dominant (by several decibels) in the HH spectrum.

4.2. Time-Dependent VV and HH Signals

In order to further study the slow and fast scatterers, we examine the slow and fast contributions separately. The VV

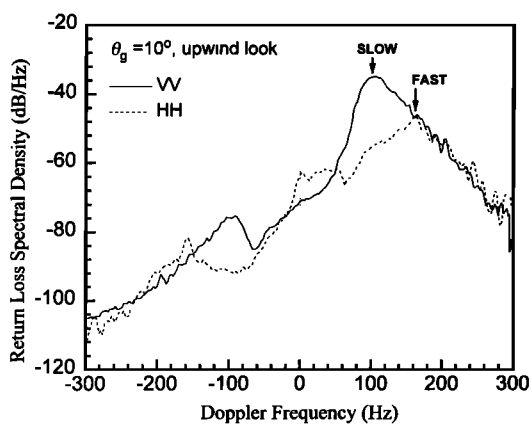

Figure 7. Time-integrated Doppler spectra of wind waves, upwind look direction, θ_g = 10°. The VV trace has higher spectral density at slow peak. Note that peak separation has occurred and HH has maximum spectral density shifted to the fast peak. The fast scatterer corresponds to the phase speed of a gravity wave of 0.97-m wavelength.

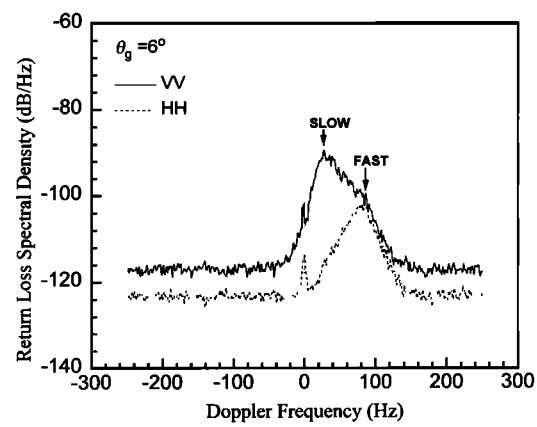

Figure 8. Royal Signals and Radar Establishment (RSRE) data from Loch Linnhe Experiment, 1989. Run 8, range cell 80. Time-integrated Doppler spectra of wind waves, upwind look direction, θ_g = 6°. The VV trace has maximum spectral density at the slow peak. Note that peak separation is complete and HH has maximum spectral density at the fast peak.

and HH scatterometer signals were band-pass filtered (with a filter half width of ~10–15 Hz) at frequencies centered about the Doppler frequency of the slow and fast peak values obtained from the time-integrated Doppler spectra (e.g., Figures 5–8) for the entire length of the return record. These record lengths were nominally 120 s for our data and 50 s for RSRE data. Henceforth, we will refer to these filtered Bragg and faster-than-Bragg signals simply as Slow and Fast signals, respectively. A few short samples of time-resolved signals are shown to indicate the characteristic features.

4.2.1. Slow (i.e., Bragg) signals. The general features for Slow return loss signals are found in both upwind and cross-wind runs. In Figures 10 and 11, two examples of 12-s records of the Slow signal for an upwind run are shown, for θ_g = 10° and 30°. Comparing the characteristic features as a function of grazing angle, we note that as the grazing angle increases, the temporal correlation ("synchronization") between HH and VV signals improves. On the average, the HH signal appears to be comparatively spikier at smaller grazing angles. This spikiness is more pronounced in the total (unfiltered) signals. The polarization ratio of the Slow signal fluctuates about some mean value but never exceeds 0 dB; i.e., HH(t) is always smaller than VV(t).

4.2.2. Fast (i.e., faster than Bragg) signals. Since no prominent Fast peaks are found in the cross-wind runs, band-passed Fast signal data are included only for upwind runs. Examples of 12-s records of the return loss Fast signal for small, medium, and large grazing angles (10°, 35°, and 70°) are shown in Figures 12, 13, and 14, respectively. The improvement in temporal "synchronization" of HH and VV signals with increasing grazing angle is again noted. The polarization ratio fluctuates about some mean value, the fluctuation being more vigorous than that seen in the polarization ratio of Slow signals. Most notable is the fact that the polarization ratio sometimes equals or exceeds 0 dB, i.e., there are instances where HH(t) ≥ VV(t). We call such instances "super" events, since HH equals or exceeds VV. As indicated by the examples shown, the occurrence of super events is not confined to small grazing angles but populates the whole range of grazing angles from 6° to 70°. Data on the probability of occurrence of HH ≥ VV events per unit antenna illumination area (i.e., footprint area) will be presented in section 6.

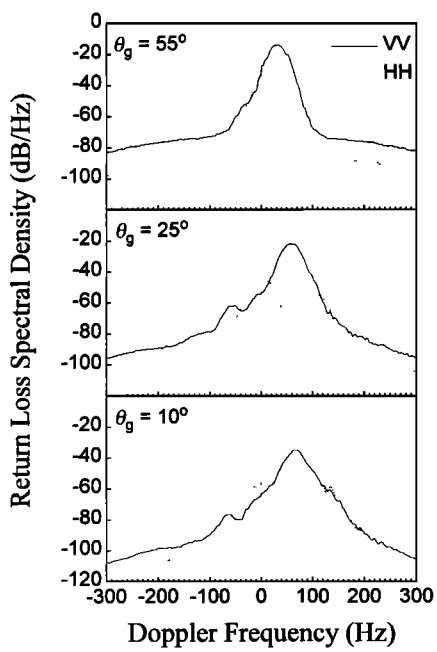

Figure 9. Time-integrated Doppler spectra of wind waves, cross-wind look direction, for θ_g = 55°, 25°, and 10°. The VV trace has higher spectral density at the slow peak. Compare these spectra with Figures 5–7 and note the absence of a prominent "fast" peak in both the VV and HH spectra.

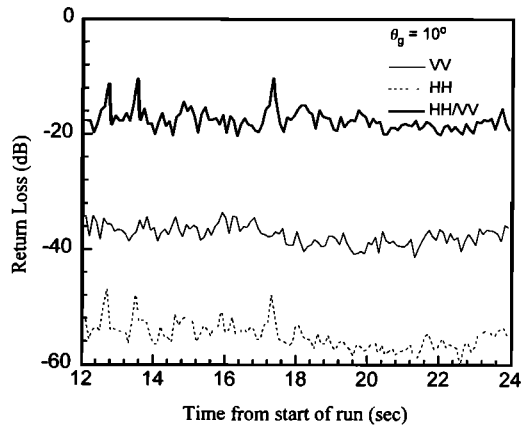

Figure 10. A short sample of time-resolved, band-pass-filtered Slow signals, upwind look direction, θ_g = 10°. Note that HH(t) and VV(t) are not well correlated in time. HH/VV never exceeds 0 dB.

4.3. Grazing Angle Dependence of Polarization Ratio

4.3.1. Slow (i.e., Bragg) signals. The time-averaged polarization ratio (HH/VV) of band-passed Slow signals versus grazing angle is shown in Figure 15. The mean value is plotted as the data point, while the standard deviation within the record is plotted as the error bar (1σ above and 1σ below the data point). The scatter for RSRE data points reflects the evaluated data for 256 range cells. For smaller grazing angles, our polarization ratio data are plotted against the effective (i.e., median) grazing angle (Appendix A). The effective grazing angle is a necessary correction because the

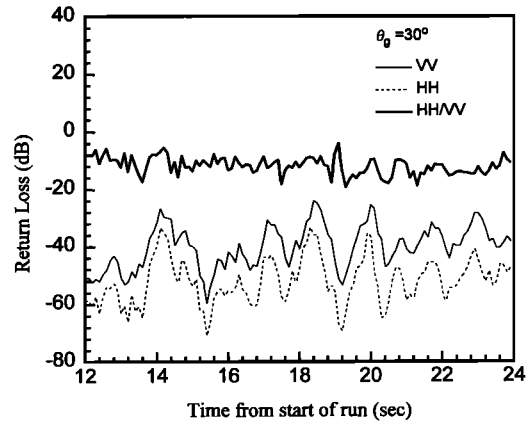

Figure 11. A short sample of time-resolved, band-pass-filtered Slow signals, upwind look direction, θ_g = 30°. Note that HH(t) and VV(t) are much better correlated in time and that HH/VV never exceeds 0 dB.

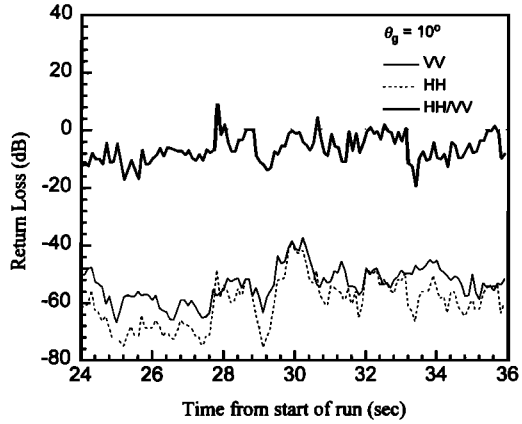

Figure 12. A short sample of time-resolved, band-pass-filtered Fast signals, upwind look direction, $\theta_g = 10°$. Note that HH(t) and VV(t) are not well correlated in time, but better correlated than the case shown in Figure 10. Note also that HH/VV occasionally equals or exceeds 0 dB. Also note that fluctuations of HH/VV about the mean value are larger than for the Slow case (Figure 10).

antenna pattern has finite beamwidth. No such correction is made for the RSRE data, since a range-resolving radar in conjunction with a 1° beam width antenna was used for the measurement. The gradual decrease in HH/VV with decrease in grazing angle is expected. Note that the cross-wind data (squares) and the upwind data (circles) are in very good agreement.

4.3.2. Fast (i.e., faster than Bragg) signals. The Fast HH(t)/VV(t) signals have also been averaged over the whole record. The mean value is plotted against the grazing angle, and the standard deviation is plotted as the error bar. The scatter for RSRE data points again reflects the evaluated data for 256 range cells. The results are shown in Figure 16. The same effective grazing angle corrections were used to plot these data. The polarization ratios for Fast signals appear to be insensitive to grazing angle and have values between −3 dB and −10 dB, with an average value of −7.45 dB and a standard deviation of ±1.86 dB.

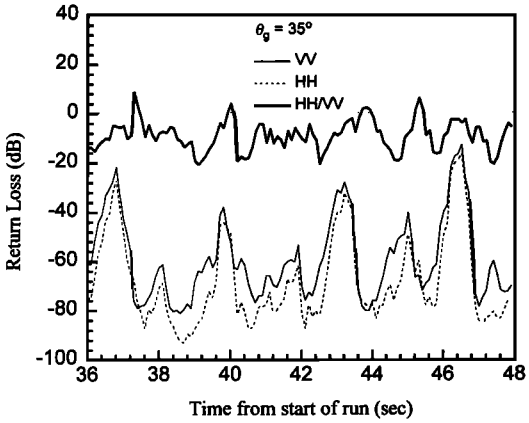

Figure 13. A short sample of time-resolved, band-pass-filtered Fast signals, upwind look direction at an intermediate grazing of $\theta_g = 35°$. Note that HH(t) and VV(t) are much better correlated in time and that HH/VV occasionally equals or exceeds 0 dB.

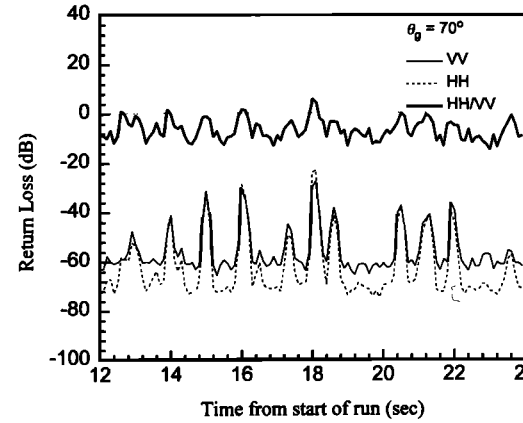

Figure 14. A short sample of time-resolved, band-pass-filtered Fast signals, upwind look direction at a large grazing of $\theta_g = 70°$. Note that HH(t) and VV(t) are much better correlated in time and that HH/VV occasionally equals or exceeds 0 dB also for this large grazing angle.

5. Comparison With Theory

5.1. Slow (i.e., Bragg) Signals

Peake [1959] used the first-order fields from *Rice*'s [1951] theory to obtain backscattered power for vertical and horizontal polarizations. The average backscatter cross sections per unit area of the ocean, of horizontal and vertical polarizations from a slightly rough dielectric surface, for an incident plane wave polarized horizontally and vertically, respectively, given by *Valenzuela* [1978], are

$$\sigma_{0(HH)} = 16\pi k_m^4 \sin^4 \theta_g \left| \frac{(\varepsilon - 1)}{[\sin \theta_g + (\varepsilon - \cos^2 \theta_g)^{1/2}]^2} \right|^2$$

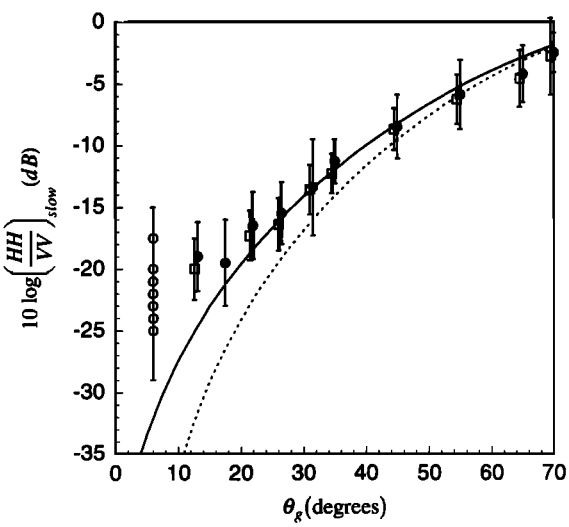

Figure 15. Time-averaged polarization ratio of Slow signals. Solid circles are TRW upwind runs, squares are TRW cross-wind runs, open circles are RSRE data. The error bar represents one standard deviation above and below the data point. The solid curve is Rice's theory with a dielectric constant appropriate for the water temperature and salinity of Loch Linnhe and the Sound of Sleat ($\varepsilon = 51.4 - i39.1$). The poor agreement of Rice's theory using a perfect conductor model is indicated by the dotted curve.

$$\cdot W(k_B, 0), \tag{4}$$

$$\sigma_{0(VV)} = 16\pi k_m^4 \sin^4 \theta_g \left| \frac{(\varepsilon - 1)[\varepsilon(\cos^2 \theta_g + 1) - \cos^2 \theta_g]}{[\varepsilon \sin \theta_g + (\varepsilon - \cos^2 \theta_g)^{1/2}]^2} \right|^2$$

$$\cdot W(k_B, 0), \tag{5}$$

where $k_m = 2\pi/\lambda$ is the microwave wavenumber, ε is the complex relative dielectric constant, W is the two-dimensional wave amplitude PSD of the surface and k_B is the Bragg-resonant wavenumber for surface waves.

Using the Debye equation [*Debye*, 1929] for the complex relative dielectric constant of a polar liquid in the microwave band, we calculated the dielectric constant of the sea water corresponding to actual temperature and salinity conditions at Loch Linnhe and the Sound of Sleat (Appendix B). For a microwave frequency of 9.3 GHz appropriate to our scatterometer, we obtain

$$\varepsilon = 51.4 - i39.1. \tag{6}$$

Our calculated relative dielectric constant differs from the oft-quoted and oft-used values of $\varepsilon = 65 - i40$ and $\varepsilon = 65 - i30.7$. The former value is from *Saxton* [1949] for $f = 10$ GHz and a water temperature of 20°C, while the latter value is from *Kerr et al.* [1947] for $\lambda = 3.2$ cm and a water temperature of 28°C. Both of these sets of values are inappropriate for our experimental conditions. It should be pointed out that the use of (6) changes the values of Rice's polarization ratio only slightly when compared with using the oft-used values. However, since the index of refraction is equal to the square root of the dielectric constant ($n = \varepsilon^{1/2}$), the amount of attenuation of the VV polarization relative to the HH polarization upon reflection will be affected by the value of n in a nonnegligible way for a double-bounce backscatter, although the value of the Brewster angle (θ_B) has only a weak dependence on n. Thus, for example, our value of dielectric constant will yield a maximum intensity ratio of $(HH/VV)_{max} = 15.5$ dB at $\theta_{g,\,min} = 7.25°$, while Kerr's value of dielectric constant will yield $(HH/VV)_{max} = 18.9$ dB at $\theta_{g,\,min} = 6.75°$, where $\theta_{g,\,min} = 90° - \theta_B$.

Using (6) for the dielectric constant, the theoretical polarization ratio (using (4) and (5) is evaluated and plotted as a function of grazing angle (solid line) in Figure 15. Also plotted for comparison is the polarization ratio for a perfect conductor (dashed line), a model sometimes favored for simplicity (Appendix C) but clearly inappropriate as is evidenced by the poor agreement with the data. Notice that Rice's theory fits the experimental data down to a grazing angle of ~20° when the appropriate dielectric constant is used. At grazing angles less than ~20°, Rice's theory begins to deviate from the experimental data. We suggest several arguments to account for the deviation.

1. During the absolute calibration of our scatterometer, we obtained cross-section measurements from geometrical objects using spheres and cylinders. A sphere is a degenerate scatterer in the sense that it does not differentiate between polarizations, whereas a cylinder is a nondegenerate scatterer in the sense that it does differentiate between polarizations. A degenerate object scatters microwaves isotropically, while a nondegenerate object scatters microwaves nonisotropically. In the process of using backscattered power measurements from cylindrical targets of diminishing radii to establish the polarization-isolation limit of our scatterometer system, we established that an alignment inaccuracy can also impose a limit on the achievable polarization isolation. The limit, for the case that the fields of both transmitted polarizations are equal in magnitude, is given by

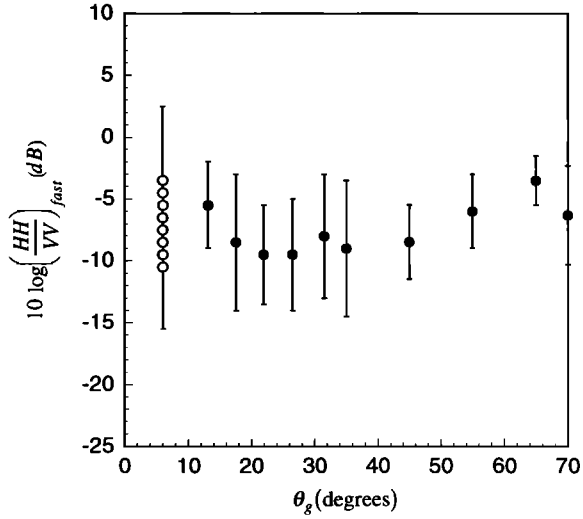

Figure 16. Time-averaged polarization ratio of Fast signals. Solid circles are TRW upwind runs; open circles are RSRE data. Although there are some physics models, there is no available theory, with predictive or postdictive capability, for Fast signals at present.

$$(HH/VV)_{limit} = 10 \log(\tan^4 \delta) \tag{7}$$

where δ is the limiting angular alignment accuracy between the vertically polarized electric field vector and the axis of a cylinder. If we conjecture that a misalignment of a nondegenerate target is limiting the polarization ratio, then a relative roll of the scattering surface (as opposed to pitch, or tilt in microwave-scattering jargon, which changes the local grazing angle) with respect to the scatterometer could impose a lower limit on the polarization ratio. However, if the −20-dB measured polarization ratio at an effective grazing angle of 13° represented a lower limit, it would correspond to a combination of boat and scattering-surface rolling at a relative angle of $\delta \approx 17°$. This value is an order of magnitude too large compared with the actual relative roll of the boat and surface. Thus boat rolling cannot be an effective mechanism for limiting the polarization ratio. On the other hand, if we adopt the two-scale Bragg model, then surface tilt could be a possible mechanism, but not at large grazing angles, since positive and negative tilt contributions would cancel. At very small grazing angles, however, Bragg patches on negatively tilted surfaces could be shadowed, resulting in an increase in the measured polarization ratio due to the positive tilting of Bragg patches. At 13° the contribution of positive tilt to the polarization ratio is 0.81 dB/degree; thus a positive surface tilt of 6.2° could account for the measured polarization ratio. However, the dominant wave slope obtained from environmental data yields a *ka* of ~0.066, which indicates a lesser surface tilt than 6.2°. Alternatively, applying composite surface theory (CST) [*Wright*, 1968; *Plant*, 1990] in a more detailed calculation (where the Bragg wave height PSD is modulated over the

longwave phase according to a prescription provided by *Miller et al.* [1991]), we can fit the data points at grazing angles 13° (−20 dB) and 6° (−25 dB) if long wave slopes were $ka = 0.15$ and 0.2, respectively. However, the large slopes required for the CST calculation to fit the experimental data are not supported by the measured environmental data (see Table 2). It is therefore quite interesting to note that for grazing angles larger than ~20°, it is unnecessary to resort to CST to fit the data (Rice's theory being adequate), while at grazing angles smaller than ~20°, application of CST using actual values of measured ka can provide only a small correction which is insufficient to match the experimental results.

2. Even if composite theory could fit the data with the appropriate slope, there is another piece of evidence which may provide deeper insight. We mentioned earlier the observation that the temporal correlation of the Slow HH(t) and VV(t) signals deteriorates with decreasing grazing angle. This result suggests that at low grazing angles, either the vertical and horizontal polarizations are sometimes obtaining returns from different patches of water (Appendix D), i.e., different locations in the "nominal" illumination spot, or are seeing returns from the same patch but with a polarization ratio value in disagreement with the prescription provided by Rice's theory or CST. Both these situations are possible if (1) there is preferential diffraction of the vertical polarization into the shadow region (the back side of a dominant wave) or (2) multipath scattering occurs. If either case were true, then $W(k_B, 0)$ would not be common to both HH and VV (see (4) and (5)). While Rice's theory (or CST) would still be correct, the usage in that form, i.e., assuming $W(k_B, 0)$ to be common to both polarizations for all times, would be inappropriate. Alternatively, if Brewster reflection is involved in the multipath scattering process, Rice's theory can still be used provided that VV is multiplied by the appropriate attenuation factor due to Brewster reflection. The effectiveness of multiple scattering in influencing backscattering microwave returns from an ocean surface is presently unclear; it is mentioned only as a possibility.

In any case, it is evident that for grazing angles smaller than ~20°, Rice's (or composite surface) theory cannot explain the Slow signal data without recourse to additional mechanisms.

5.2. Fast (i.e., Faster Than Bragg) Signals

To explain the Fast signals, concepts previously introduced, such as two-scatterer models, scattering from breaking waves, or returns from the tips of dominant waves, bound waves, plumes, facets etc. [*Wetzel*, 1977, 1986; *Kwoh and Lake*, 1984; *Jessup et al.*, 1991a; *Ebuchi et al.*, 1993] seem to be slowly gaining acceptance. It is uncertain whether any useful theory, with either predictive or postdictive capability, is available at the moment. However, vigorous efforts toward construction of a realistic theory are in progress [*Caponi et al.*, 1993]. It is certain from review of the data presented so far that there are other scattering mechanisms besides Rice's mechanism and the composite-surface model. In essence, we have the following experimental results from the Fast signals: (1) After accounting for the wind drift, platform speed, etc., the Doppler frequency of the Fast signal corresponds to a velocity which far exceeds the Bragg-resonant wave phase speed. (2) The time-averaged polarization ratio of the Fast signal is roughly constant, ranging between −3 dB and −10 dB, and is insensitive to grazing angle. (3) The time-resolved polarization ratio HH(t)/VV(t) of the Fast signal can occasionally equal or exceed unity. Each of these results is in violent disagreement with Rice's theory. It is tempting to argue that the large values of polarization ratio from fast scatterers can be accounted for using only bound Bragg waves [*Duncan et al.*, 1974] tilted at the appropriate slope of some substrate wave to yield results which can be described by CST. The weakness with this argument is that if bound Bragg waves were the only scattering mechanism, then all values of instantaneous polarization ratio would be bounded by an upper limit of 0 dB. The occurrence of super events with polarization ratios greater than 0 dB in the experimental data provides convincing support that bound Bragg waves are not the only contributors to fast scatterers.

What mechanisms may give rise to the observed data? The first result points to returns from scatterers associated with a faster wave, that is, a water wave of much longer wavelength than the Bragg-resonant wave. The second result points to possible returns from wave-breaking (incipient or otherwise) of the longer waves and from "specular facets" (Appendix E) associated with the longer wave. The third result points to either nondegenerate objects whose orientations favor the horizontal polarization return, or multipath scattering in which one reflection occurs at the Brewster angle so that the vertical polarization return is substantially attenuated. It should be stressed, however, that most of the time, VV is observed to dominate over HH.

On the second point mentioned above, "longer wave" simply means a wave much longer than the Bragg wave. It could be a strained shorter gravity wave and need not be the dominant wave in the wind wave field. As a matter of fact, the phase speed data obtained through the Doppler spectra indicate that fast scatterers are associated with gravity waves with wavelengths substantially shorter than the dominant waves for each case. This can be seen by comparing the gravity-wave lengths given in the captions of Figures 5, 6, and 7 with the dominant wave lengths which can be calculated from f_{dom} given in Table 2. The result of this observation in the ocean is different from results obtained from laboratory experiments, where fast scatterer speed usually can be associated with the phase speed of the dominant wave in the wave tank [*Lee*, 1976; *Ebuchi et al.*, 1993]. Apparently, in an ocean environment, the X band scatterometer is a good detector of the waves most likely to break. The result of the field observation raises an interesting question: What is the wave most likely to break in a given ocean wind wave field?

Before embarking on further discussions of mechanisms giving rise to fast scatterers, more data are presented in the following section to support the above conjectures.

6. Additional Data and Discussion

6.1. Time-Resolved Doppler Spectra

Of the many sequences of time-resolved Doppler spectra available in our data that strongly support the mechanisms which we have suggested as giving rise to the Fast signals, we offer one example. Figure 17 shows a 12-s portion of a total (i.e., not band-pass filtered) temporal record of the return-loss signal at $\theta_g = 10°$. As noted earlier, the HH

returns are "spikier" at low grazing angles, and this is obvious from the figure.

Eight frames of Doppler spectra taken from the record (Figure 17), from t = 16.6 s to t = 18.0 s at 200-ms intervals, are shown in Figure 18. The Slow (f_S) and Fast (f_F) Doppler frequencies, obtained from the time-integrated Doppler spectrum (Figure 7), are marked by arrows. At time t = 16.6 s, the Fast part of the spectrum has no energy. In the next two frames, t = 16.8 s and 17.0 s, spectral energy contributions from fast scatterers are evident. Notice that in the Fast portion of the spectrum at t = 16.8 s, HH ~ VV; at t = 17.0 s, HH > VV, and at t = 17.2 s, VV ≫ HH. At time t = 17.0 s and later frames, notice how the spectral density at the Fast frequency "cascades" down toward the Slow frequency, thus filling in the spectrum of frequencies between f_F and f_S. Again, at t = 17.6 s, HH ≫ VV, followed by HH ~ VV (t = 17.8 s), then HH < VV (t = 18.0 s), and again accompanied by a cascade of energy from f_F to f_S.

The various features observed in the eight frames of Doppler spectra in Figure 18 may represent the scatterometer returns from an incipient wave-breaking or microbreaking process. A possible hydrodynamic scenario is sketched out in a cartoon in Figure 19, in which the vertical scale is greatly exaggerated. At time step 1, the scatterometer sees free Bragg waves and the Doppler frequency corresponds to the Bragg wave phase speed. At time step 2, breaking is just about to occur on the forward face of the fast wave. This could form a degenerate scatterer which does not distinguish polarization, or it could form a nondegenerate scatterer which favors either the VV or HH polarization. However, the Doppler frequency will correspond to the phase speed of the fast wave. At postbreaking time steps 3, 4, and 5, a bore may form, or by-products of the "broken" wave (plumes [*Wetzel*, 1986], foam, bubbles, and shorter waves) may be "trapped" temporarily at the crest vicinity of the fast wave and eventually be shed by the fast wave and left behind. This results in a variety of scatterers which at first exhibit the fast wave phase speed but eventually decelerate to the free Bragg wave phase speed if they are able to survive the transition. Thus one should observe the "cascading" of the Fast

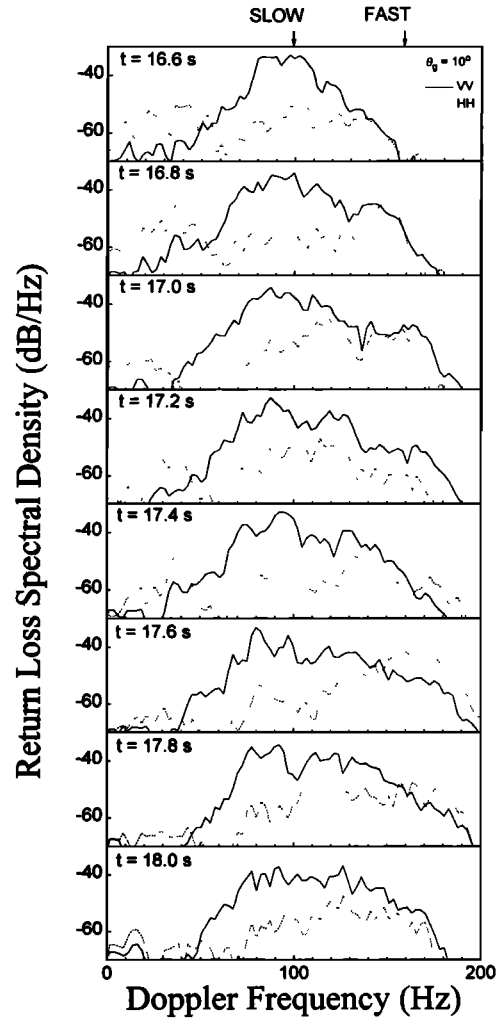

Figure 18. A sequence of time-resolved Doppler spectra depicting how horizontal and vertical polarizations occasionally indicate Fast returns. Note that in the Fast region, it is possible for HH to equal or exceed VV. Also note energy in "cascade" frequencies. Refer to text for description.

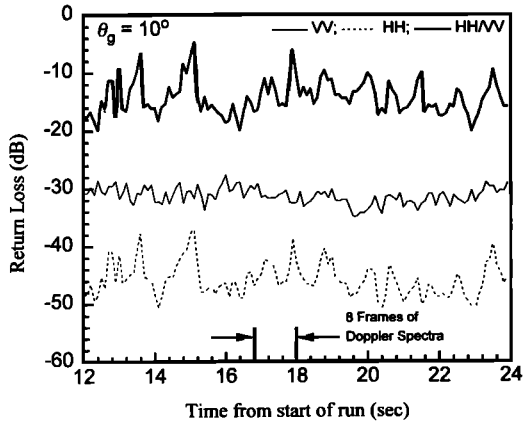

Figure 17. A 12-s sample record of the total signal for an upwind run, θ_g = 10°. The lower trace is HH, the middle trace is VV, and the top trace is HH/VV. Note that HH appears to be spikier. Between the time of 16.6 s and 18.0 s, eight frames of Doppler spectra will be shown in Figure 18.

Doppler frequency to intermediate frequencies and finally to the Slow Doppler frequency. Although the actual data do not have an exactly one-to-one correspondence with the steps in the idealized scenario, certain features described above can be seen in the sequence of time-resolved Doppler spectral data. Time-resolved Doppler spectra exhibiting occasional large Doppler shifts have also been observed and have been attributed to signatures of breaking waves by *Jessup et al.* [1991a].

6.2. Wind Direction Dependence of Doppler Spectra

The upwind and cross-wind spectral data have already underscored the fact that ocean backscatter is not isotropic. This is easy to understand, since waves propagate and also break, predominantly in the wind direction. For cross-wind look, the scatterometer does not see (or very seldom sees) breaking waves and therefore does not show a prominent Fast component in the Doppler spectra.

An additional set of data in support of our arguments as to the identification of scattering mechanisms is presented in Figure 20. This set was obtained by running the boat in a

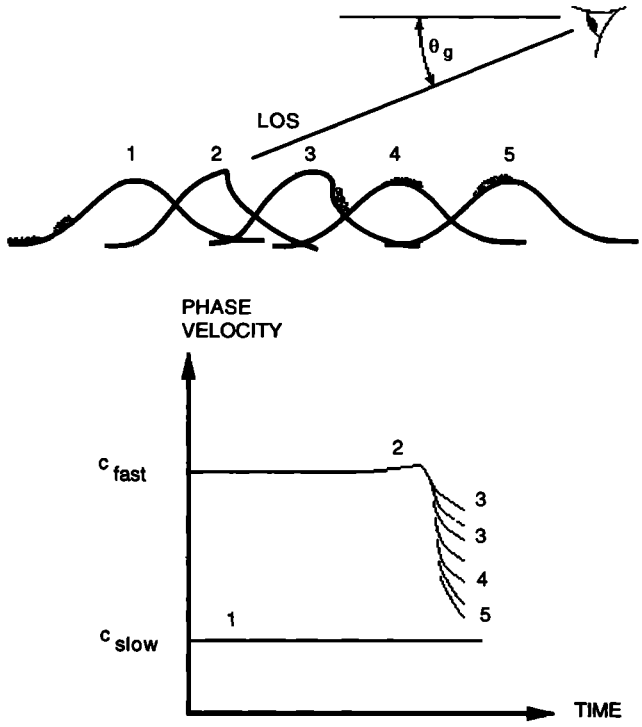

Figure 19. A possible scenario which can produce certain aspects of the time-resolved series of Doppler spectra shown in Figure 18. The top cartoon is a depiction of the various stages of an incipient wave-breaking process, where the vertical scale is greatly exaggerated (LOS, line of sight). The evolution of the scatterer speed of the various types of scatterers is given qualitatively in the bottom phase velocity versus time graph.

clockwise circle in presumably the same wind wave field. The bore sight grazing angle of the scatterometer was fixed at $\theta_g = 35°$. The simultaneous boat and wind speeds (v_b and U_{10}, respectively) for each boat heading ϕ with respect to the wind direction are provided below.

The Doppler spectra are 20-s averages, with boat headings shown at 45° intervals with respect to the wind direction. Starting from $\phi = 0°$ or 360° ($v_b = 0.8$ m/s, $U_{10} = 9.5$ m/s) the Slow peak is at ~75 Hz and the Fast peak is at ~125 Hz. Notice that the Slow peak is dominant for the HH spectrum, since the grazing angle used is larger than the switch-over angle. At the next heading, one sees the $\phi = 45°$ ($v_b = 0.7$ m/s, $U_{10} = 11$ m/s) case where both port and head wind components are present; both the Slow and Fast components are still present, but the Fast component is diminished in power. In the cross-wind case ($\phi = 90°$, $v_b = 0.7$ m/s, $U_{10} = 9.5$ m/s) in which only the Slow component is evident, the Fast spectral components at ~110–140 Hz have practically disappeared (40 dB lower compared with the 0° case). The cases between $\phi = 135°$ to 225° (at 135°, $v_b = 1.15$ m/s, $U_{10} = 9$ m/s; at 180°, $v_b = 1.15$ m/s, $U_{10} = 10.5$ m/s; at 225°, $v_b = 1.15$ m/s, $U_{10} = 9.5$ m/s) all have stern wind components as well as fast waves propagating away from the scatterometer; therefore the spectra contain scattering from receding elements and are thus shifted to lower frequencies. In the case in which the boat is running with the wind ($\phi = 180°$, bottom spectrum), there is partial blocking of the fast waves as well as the wind by the boat, and the scatterometer sees predominantly randomly distributed Bragg waves. The peak at around −20 Hz could be due to scattering from parts of a receding long wave of 1.8-m wavelength or from an unidentified object, perhaps a waterfowl, that was moving away at 1.68 m/s. Another cross-wind case is encountered at $\phi = 270°$ ($v_b = 1.1$ m/s, $U_{10} = 7.5$ m/s) where Fast components are absent. The case at $\phi = 315°$ ($v_b = 0.9$ m/s, $U_{10} = 9$ m/s) again has a head wind component and with it the reappearance of Fast components in the Doppler spectra. It should be pointed out that the Doppler spectra are short time (~20 s) averages and that the boat speed as well as the wind speed varied during the course of the circle run (as seen from simultaneous recordings of the temporal wind speed and boat speed); therefore one should not expect the Doppler spectra of the two cross-wind (port and starboard wind) runs to be exactly identical. The same general features were verified in another circle run (this time, counterclockwise) in a different wind wave field and at a smaller grazing angle, but we refrain from showing the data in the interest of brevity.

The circle run data thus further substantiate the several suggested backscattering mechanisms from wind wave surfaces.

6.3. Probability of "Super" Events

Returning to the topic of "super" events mentioned earlier in section 4.2.2, recall that the definition refers to instances when $HH(t) \geq VV(t)$ and occurs only for Fast signals. Strict adherence to Rice's theory would render such a result impossible, since according to this theory, HH should always be less than VV unless at normal incidence (i.e., 90° grazing angle), where backscatter theoretically becomes independent of polarization (Appendix F). However, if one accepts the notion that there exist nondegenerate scattering objects which are capable of preferentially scattering horizontally polarized radiation, then super events are natural. To find out how natural they are, we quantify super events by providing a measure of their occurrence.

In Figure 12, at time $t = 27.5$ s, one observes a "super" event which lasts for roughly 0.2 s. Similarly, such events are seen at $t = 27.8$ s, 28.5 s, 30.5 s, and so on throughout the record. For time-resolved, band-passed Fast signals at each grazing angle, we sum the duration of all such super event occurrences ($\Sigma\Delta t$), then divide this time by the total length of the record (T) and by the illumination area A_{FP} (i.e., the antenna footprint area, which is πab, where a and b are given in Table 2) to obtain the probability of occurrence of super events per unit antenna footprint area

$$P = \frac{\Sigma\Delta t}{TA_{FP}}. \tag{8}$$

Figure 21 shows P plotted as a function of grazing angle (P has dimensions of reciprocal square meters). The solid points are our data, and the open points are RSRE data. The value of P is dependent on filter band width, which for the present case is ~20 Hz. We find an approximate exponential dependence of P with respect to grazing angle, giving

$$P = \frac{1}{B} \exp\left(\frac{\theta_g}{\theta_0}\right) \tag{9}$$

with parameters $B = 2 \times 10^3$ m^2 and $\theta_0 = 14.89°$ providing the best fit. The triangular data point does not fall on the

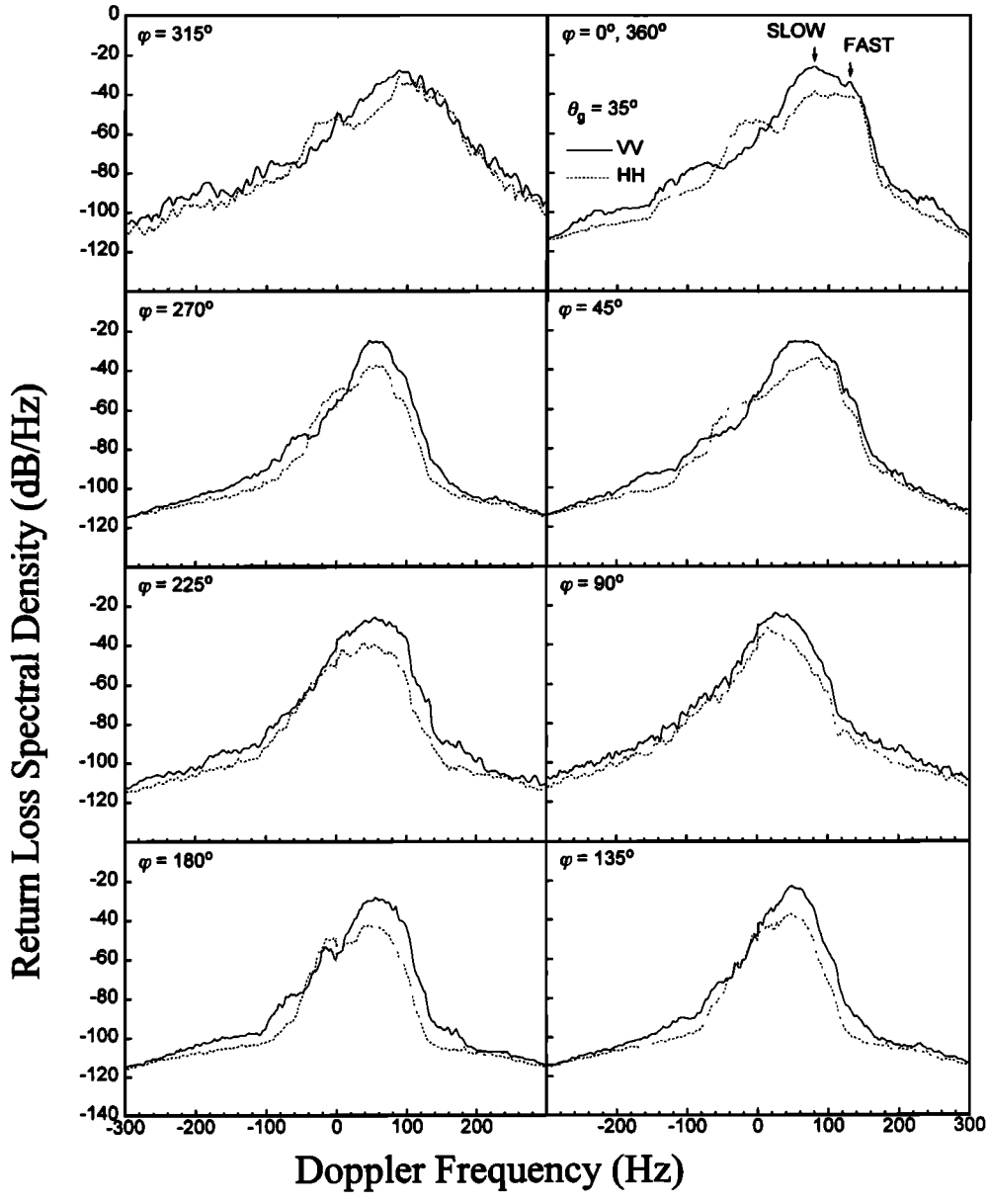

Figure 20. Doppler spectra as a function of wind direction. This circle run sequence was conducted at a fixed grazing angle of $\theta_g = 35°$. Doppler spectra at 45° intervals with respect to the wind direction are shown. The data set starts and ends with the upwind orientation ($\varphi = 0°$ and at $\varphi = 360°$).

curve. However, if we look up Table 2 for this particular run, we find that the wind speed (5 m/s) is the lowest of all the runs. This would indicate that the probability of occurrence of super events may be a function of sea state and thus of wind speed and fetch. Further investigation is required.

For large grazing angles it should be obvious that the probability of scattering from specular facets (whether degenerate or nondegenerate) will be much higher than at low grazing angles simply because the distribution of water surface slopes strongly favors the smaller slopes. This can be a partial explanation for the data in Figure 21. The results also indicate that in the range of wind speeds between 5 and 13.5 m/s for which these data were obtained, super events are rather rare (i.e., VV > HH most of the time). However, the occurrence of super events at low grazing angles is sufficient to raise the time-averaged polarization ratio to values which greatly exceed the values prescribed by Rice's theory, thus lending support to the conjecture that the scattering is from objects other than gratinglike patches of Bragg waves. Since Bragg scattering provides very little return of horizontally polarized radiation for low grazing angles, super events can be important and in fact become the dominant contributor to the returns for horizontal polarization, in spite of their low probability of occurrence.

Super events have also been observed by *Jessup et al.* [1991a] in field experiments. However, they attribute super events as possibly due to wedge scattering [*Lyzenga et al.*, 1983], random fluctuations in the independent measurements, or the effect of averaging. Their reasoning is that the dominance of HH over VV is "not consistent with analytical models for which Bragg scattering dominates" [*Jessup et al.*, 1991a, p. 20,551]. While wedge scattering is a possibility

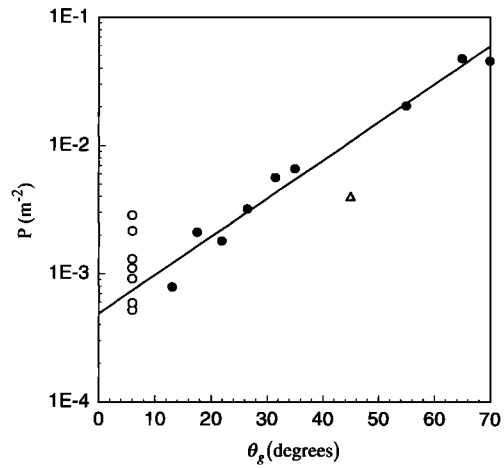

Figure 21. Probability of super events per unit footprint area as a function of grazing angle. Solid circles are TRW data, open circles are RSRE data. The triangle is a run at the lowest wind speed. The straight line is a least squares fit to the solid circles.

(and in principle can be verified by checking the cross sections, polarization ratios, and Doppler velocities), we are quite skeptical that it is due to random fluctuations or the effect of averaging, since we believe that an a priori assumption that Bragg scattering has to dominate under all circumstances appears to be neither justified nor supported by experimental data.

6.4. Comparison of Backscattering Cross Sections

In order to compare Bragg scattering cross sections with cross sections due to non-Bragg mechanisms (e.g., specular facets), we provide a simplified estimation by comparing the cross sections per unit of area of ocean from pure specular reflection with the Bragg scattering for, say, horizontal polarization. By pure specular reflection it is assumed, for the sake of argument, that the return is from a large flat surface of water with its surface normal in the direction of the bore sight grazing angle. We have

$$\frac{\sigma_{\text{PURE SPECULAR}}}{\sigma_{\text{BRAGG SCATTER (HH)}}} \sim \frac{\sin\theta_g |R_F|^2}{\sigma_{0(\text{HH})}}, \tag{10}$$

where R_F is the Fresnel reflection coefficient for normal incidence (i.e., 90° grazing angle)

$$R_F = \frac{\varepsilon^{1/2} - 1}{\varepsilon^{1/2} + 1} \tag{11}$$

where ε is the computed relative dielectric constant given by (6) and $\sigma_{0(\text{HH})}$ is given by (4). To evaluate (10), we need to know the value of the product of the fourth power of the microwave wavenumber and the Bragg-resonant two-dimensional wave height PSD, i.e., $k_m^4 W(k_B, 0)$. Comprehensive two-dimensional wave height power spectral density data were obtained from surface slope data measured during the experiment using our scanning laser slope gauge [*Lee et al.*, 1992; *Barter et al.*, 1992b, c]. Our data show that values of $W(k_B, 0)$ are dependent on wind speed and wind direction, with the grazing angle dependence being implicit in the Bragg wavenumber. As an example, for a wind speed of 10.9 m/s, for an upwind direction, our measurement yields

$$k_m^4 W(k_B(\theta_g), 0) \approx 4.8 \times 10^{-5}. \tag{12}$$

Inserting the appropriate values into (10), we find that at 10° grazing angle, the pure specular reflection cross section is larger than the horizontally polarized Bragg scattering cross section by a factor of $\sim 8 \times 10^4$. In other words, in an antenna footprint of say, 50 m^2, a 6 cm^2 purely specular area would provide the same backscattered power as the horizontally polarized Bragg return from the entire footprint. Generally, however, non-Bragg cross sections are expected to be smaller than pure specular cross sections; a pure reflector model is used in this example only to provided an upper limit for the estimation of non-Bragg-scattering cross sections. In principle, the cross section due to any non-Bragg-scattering mechanism could be calculated if the size, shape, and orientation of the particular scattering object were known. The present example serves to illustrate that only a small fraction of the antenna footprint area is required for non-Bragg-scattering mechanisms to provide a nonnegligible return. The fraction can be anywhere in the range of 10^{-2}–10^{-5}, depending on the facet geometry as well as the wind speed, wind direction, microwave polarization, and grazing angle.

6.5. Coherence Properties of Scatterers

The coherence properties of scatterers in the antenna footprint of a CW scatterometer can provide clues to the nature of the scattering processes. The study of the problem, however, is complicated by the fact that (1) there are different types of scattering mechanisms (e.g., Bragg and specularlike), (2) there is a distribution of the size of the scatterers, (3) the scatterers can have different lifetimes, and (4) there can be a distribution of scatterer speeds. Nevertheless, we will attempt to gain some insight by examining two idealized cases which we will use as simple models.

The normalized autocorrelation function of the backscattered field is given by

$$\gamma_{ii}(\tau) = \frac{\langle E_i^*(t) E_i(t+\tau)\rangle}{\langle E_i^*(t) E_i(t)\rangle}, \tag{13}$$

where $E(t)$ and $E^*(t)$ are the complex amplitude and its complex conjugate, respectively, of the backscattered field; τ is the lag time; the subscript i refers to either vertical or horizontal polarization; and angle brackets denote temporal average. We examine the following two special cases.

6.5.1. Case 1: Lifetime-dominated scattering. Assume that all scatterers (patches or facets) are of the same size and are moving at the same speed, then the scattered field from the nth scatterer can be expressed as

$$E_n(t) = E e^{(i\omega_0 t + i\theta_n)} e^{-(t/2\tau_e)}, \tag{14}$$

where ω_0 is the scattered frequency, θ_n is the phase which is assumed to be random, and τ_e is the average lifetime of the scatterer (i.e., the one e-folding time of the backscattered power). The normalized autocorrelation function, using equation (13), is thus

$$\gamma_{ii}(\tau) = e^{i\omega_0\tau} e^{-(|\tau|/2\tau_e)}. \tag{15}$$

The absolute value of γ_{ii} will yield an exponential decay behavior with respect to the lag time.

6.5.2. Case 2: Scattering dominated by scatterers with Gaussian distribution of speeds. Assume that the scatterers are of the same size but the scatterer lifetimes are sufficiently long that the process is not lifetime dominated. Assume that the scatterers are moving at different speeds, the distribution of which is assumed to be Gaussian. For this case, the scattered intensity (i.e., the power spectral density, or the Doppler spectrum) is given by

$$P(\omega) = \frac{1}{\pi^{1/2}\omega_E} e^{-(\omega-\omega_c)^2/\omega_E^2}, \tag{16}$$

where ω_c is the center frequency (e.g., the peak of the Doppler spectrum) and ω_E is the width at the one e-folding point in the spectrum. Since the autocorrelation function is the Fourier transform of the power spectral density

$$G(\tau) = \int_{-\infty}^{\infty} P(\omega) e^{i\omega\tau} d\omega, \tag{17}$$

it is straightforward to compute the normalized autocorrelation function by noting that

$$\gamma_{ii}(\tau) = \frac{G(\tau)}{G(0)}. \tag{18}$$

Using expressions (16) to (18), one obtains

$$\gamma_{ii}(\tau) = e^{i\omega_0\tau} e^{-(\tau/2\tau_E)^2}, \tag{19}$$

where $\tau_E \equiv \omega_E^{-1}$. In this case, the absolute value of γ_{ii} is Gaussian with respect to lag time.

Comparing equations (15) and (19), one notes that the shapes of the normalized autocorrelation function for the two cases are entirely different. Also, the slopes at zero lag time are different: for case 1, $d|\gamma|/d\tau = -0.5\tau_e^{-1}$, while for case 2, $d|\gamma|/d\tau = 0$.

A model based on the two special cases predicts that at large grazing angles, Bragg scattering dominates over scattering from fast events for both polarizations; the returns should therefore be characterized mainly by the spread in scatterer velocity, and thus the shape of the normalized autocorrelation function for both polarizations should be similar. At small grazing angles, in addition to Bragg scattering, the returns are also strongly influenced by scattering from fast events (probably from wave crests of longer waves) which occur sporadically in time. The scattering can thus be "lifetime dominated" as well. Since the horizontal polarization will be affected more than the vertical polarization, the normalized autocorrelation function should therefore be narrower in width for the horizontal than for the vertical polarization.

Examples of our data are shown for small, medium and large grazing angles, and both upwind and cross-wind configurations. In Figure 22, for an upwind look at 10° grazing angle, we see the difference between the horizontal and vertical polarizations by noticing that $|\gamma_{HH}(\tau)|$ is narrower than $|\gamma_{VV}(\tau)|$, with a one e-folding time of ~4 ms (which could be an average facet lifetime) for the horizontal polarization. Examination of recorded video images of the footprint reveal microwave-breaking events which can sometimes be observed in one frame and not in the next frame 33 ms later. When model exponential and Gaussian curves are fitted through the one e-folding point of the autocorrelation data for each polarization, we find that the normalized autocorrelation function is bracketed between these model limits. In Figure 23, for an upwind look at 25° grazing angle, the difference between the horizontal and vertical polarizations is also quite apparent with $|\gamma_{HH}(\tau)|$ decorrelating faster than $|\gamma_{VV}(\tau)|$. At short lag times, $|\gamma_{HH}(\tau)|$ is almost Gaussian but deviates from Gaussian in a small bump peaked at around $\tau = 0.019$ s. The inverse of this lag time is ~53 Hz, which is the separation between the Bragg peak and the fast peak in the Doppler spectrum of the HH polarization (see Figure 6). The autocorrelation function of the vertical polarization is practically Gaussian. In Figure 24, for an upwind look at 55° grazing angle, the shapes of the autocorrelation functions of the horizontal and vertical polarizations are quite similar. At short lag times, both $|\gamma_{HH}(\tau)|$ and $|\gamma_{VV}(\tau)|$ are almost Gaussian but deviate from Gaussian in a small a bump peaked at around $\tau = 0.026$ s. The inverse of this lag time is ~39 Hz, which is the separation between the Bragg peak and the fast peak in the Doppler spectrum of both the HH and VV polarizations (see Figure 5). In Figure 25, for a cross-wind look at 10° grazing angle, the horizontal polarization result is Gaussian at short lag times with a gentle bump (beyond 0.008 s) which raises the curve and connects it to the exponential at a lag time of 0.012 s. This is due to the weak but not negligible influence of the fast scatterers (see the 10° case in Figure 9). The vertical polarization result is between a Gaussian and an exponential but closer to the former. Note that $|\gamma_{HH}(\tau)|$ is narrower than $|\gamma_{VV}(\tau)|$. In Figure 26, for a cross-wind look at 25° grazing angle, the horizontal polarization result is between a Gaussian and an exponential while the vertical polarization result is between a Gaussian and an exponential but much closer to the former. Note that $|\gamma_{HH}(\tau)|$ is only slightly narrower than $|\gamma_{VV}(\tau)|$. In Figure 27, for a cross-wind look at 55° grazing angle, both the horizontal polarization and vertical polarization results are practically Gaussian, and $|\gamma_{HH}(\tau)|$ and $|\gamma_{VV}(\tau)|$ are equal in width. The decorrelation times match the Doppler band widths in the corresponding Doppler spectra. For example, for the 55° cross-wind case, the decorrelation time at half value is $\tau = 0.012$ s. From $\exp[-(2\pi\Delta f\tau/2)^2] = 1/2$, one calculates a −3-dB Doppler width of $\Delta f = 22$ Hz, which matches the observed band width in the Doppler spectrum (see 55° cross-wind Doppler spectra in Figure 9).

In general, we have the following observations: for cross-wind cases at large grazing angles where there is very little contribution from fast scatterers, the normalized autocorrelation functions for both polarizations are practically identical and Gaussian in shape. For smaller grazing angles in both upwind and cross-wind configurations, γ_{HH} is usually narrower than γ_{VV}, i.e., γ_{HH} decorrelates faster than γ_{VV}, and both curves lie between the exponential and Gaussian limits, indicating that scattering from a mixture of mechanisms could be playing a major role. By and large, the qualitative difference between the normalized autocorrelation functions of HH and VV is usually more apparent for upwind cases, especially at low to intermediate grazing angles.

The results of the autocorrelation functions obtained at various configurations indicate that the coherence properties of scatterers are quite complex. This is especially obvious

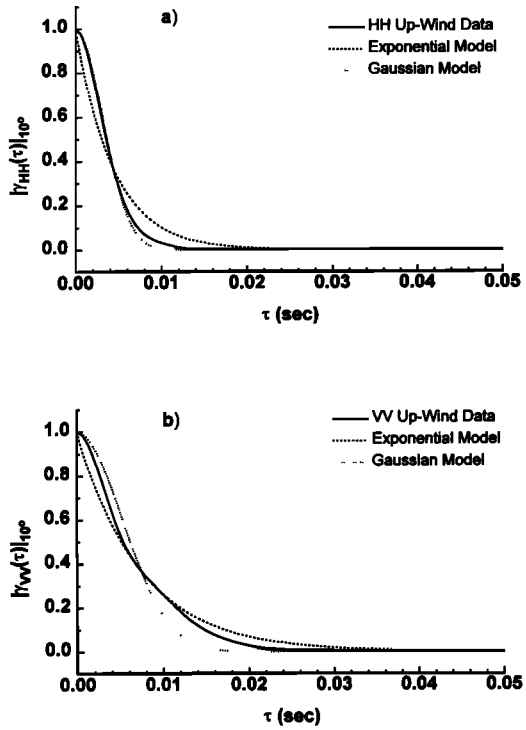

Figure 22. The normalized autocorrelation functions of the (a) horizontal and (b) vertical polarizations versus lag time. Upwind look, $\theta_g = 10°$. Note that both $|\gamma_{HH}|$ and $|\gamma_{VV}|$ are bracketed by the exponential and Gaussian models.

for upwind look configurations, where different scattering mechanisms are indicated by the structures and different timescales in the autocorrelation functions. There is an important issue which needs to be mentioned when dealing with autocorrelation functions. Any instrumental artifacts of the scatterometer, if not removed prior to computation of $|\gamma_{ii}(\tau)|$, will contribute to structures in the autocorrelation function. An example is shown in Figure 28, where the result of the raw data (which includes the artifacts) is compared with the result of data with artifacts removed. The difference between $|\gamma_{HH}(\tau)|$ for cross-wind look at 25° with and without the low frequency artifact (see text description of Figures 4 and 9) is quite obvious. In Figure 28 the plateau at around lag time of ~0.01 s is a manifestation of the instrumental artifact. In general, instrumental artifacts are easier to detect in Doppler spectra than in autocorrelation functions.

The general features we observe are in quantitative agreement with data obtained by *DeLoor and Hoogeboom* [1982], e.g., the short decorrelation time at the initial decay of $|\gamma_{ii}(\tau)|$ of the order of 10 ms or less and the increase of decorrelation time with increasing grazing angle. Recalling that the ocean is an anisotropic scatterer (we have shown through many examples that the Doppler spectra and autocorrelation functions are wind direction and grazing angle dependent), no quantitative comparison can be made with their data, however, since their conclusions are based on averages over all wind directions and over a fairly large range of grazing angles. The bumps we observe in our autocorrelation data are different from the oscillations at very long delay times (many seconds) seen by *Ward et al.* [1990]. In our case we attribute the bumps to a different scattering mechanism, while in the case of *Ward et al.* [1990]

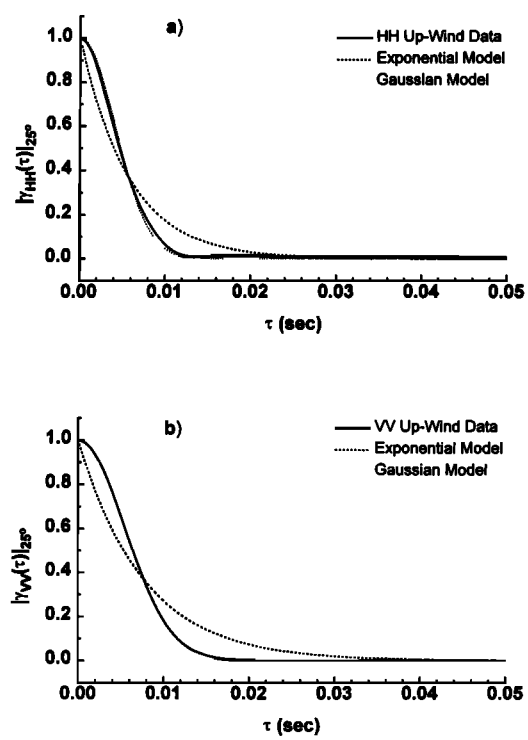

Figure 23. The normalized autocorrelation functions of the (a) horizontal and (b) vertical polarizations versus lag time. Upwind look, $\theta_g = 25°$. Note that $|\gamma_{HH}|$ is narrower than $|\gamma_{VV}|$. See text for description.

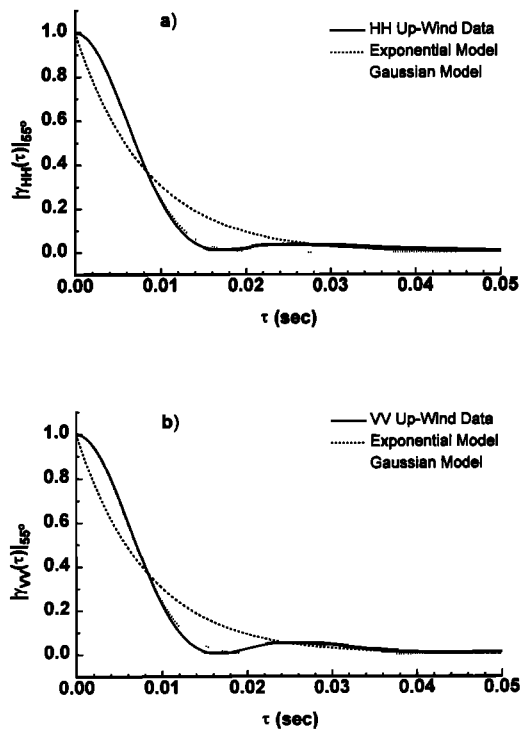

Figure 24. The normalized autocorrelation functions of the horizontal and vertical polarizations versus lag time. Upwind look, $\theta_g = 55°$. Note that both $|\gamma_{HH}|$ and $|\gamma_{VV}|$ have similar structure. See text for description.

it is stated that the slower periodic decay may be associated with modulations of Bragg scatterers. In any case, wherever structures such as plateaus and bumps in the autocorrelation functions are seen, it is possible to speak of different timescales. Besides the fact that one particular scattering mechanism (Bragg scattering) can be modulated in time by long waves, thus giving rise to the different timescales, we believe that the complex structures in the autocorrelation functions could also point to different scattering processes. If different scattering processes are the cause of complex structures of autocorrelation functions, then relating decorrelation time to Doppler band width should be done in a consistent way which is physically meaningful. For example, if the autocorrelation function is Gaussian, then the decorrelation time is a band width which corresponds to a spread in speeds. If it is exponential, then the decorrelation time is representative of a scatterer lifetime. However, if the autocorrelation function is neither exponential nor Gaussian, then the decorrelation time is representative of neither scatterer lifetime nor a spread in scatterer speed. Therefore in order to associate the decorrelation time with something which is physically meaningful, one needs to identify the actual scattering process.

We have found that coherence properties in general and autocorrelation functions in particular are strongly grazing angle and wind direction dependent, as exhibited in the examples we have shown. We believe that different scattering mechanisms can be a major cause of the complex nature of the autocorrelation function.

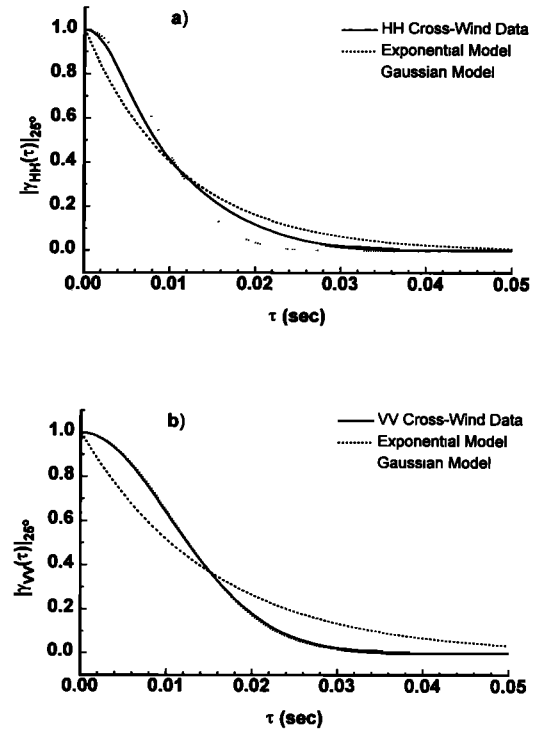

Figure 26. The normalized autocorrelation functions of the horizontal and vertical polarizations versus lag time. Cross-wind look, $\theta_g = 25°$. Here $|\gamma_{HH}|$ is narrower than $|\gamma_{VV}|$; the former is bracketed by the exponential and Gaussian models, while the latter is practically Gaussian. Note that both $|\gamma_{HH}|$ and $|\gamma_{VV}|$ are wider than the 25° case for upwind look.

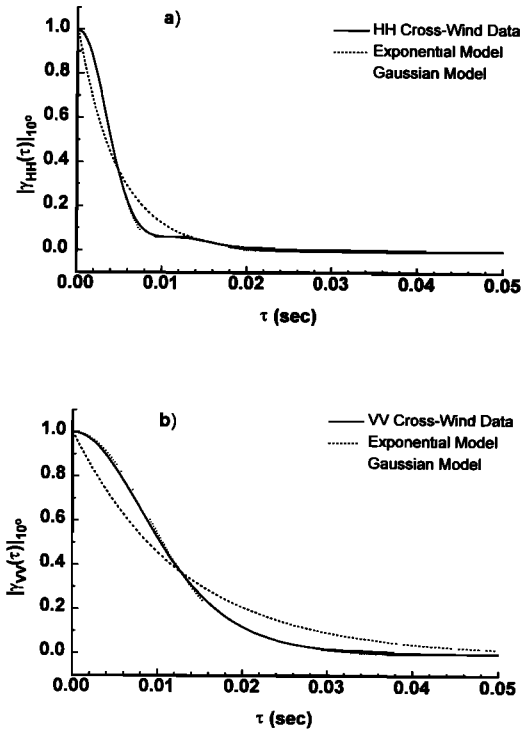

Figure 25. The normalized autocorrelation functions of the horizontal and vertical polarizations versus lag time. Cross-wind look, $\theta_g = 10°$. Here $|\gamma_{HH}|$ is narrower than $|\gamma_{VV}|$; both and are bracketed by the exponential and Gaussian models. Note that $|\gamma_{VV}|$ is wider than the 10° case for upwind look.

6.6. Spiking

"Spiking" (sometimes also called a "burst") has become a topic of some interest in recent years [*Jessup et al.*, 1990, 1991b]. It has been described by *Trizna et al.* [1991] as a radar scattering event at grazing angles less than 10° associated with scattering caused by the crest of a steep or breaking fast wave, and it is distinguished by its rare occurrence and very large values of HH/VV.

We find in our data ample evidence to suggest that the term "spiking" requires a broader and at the same time clearer definition. There are instances when spiking is observed even in the Slow signal. For example, in Figure 10, spiking occurs in the HH signal (at $t = 12.5$ s, 13.4 s and 17.2 s). However, since HH < VV, we find that spiking does not necessarily produce a super event; also, since it is a Slow signal (the Doppler frequency corresponds to a Bragg wave), it cannot be associated with a breaking faster-than-Bragg wave. On the other hand, in cases where HH > VV, we find that super events are not necessarily due to spiking; for example, see Figure 13, at $t = 37.2$ s. Furthermore, the occurrence of super events is by no means restricted to small grazing angles as shown in the examples of Figures 12–14. We also observe "negative spiking"; for example, in Figure 12, at time $t = 33.2$ s, VV increases upward while HH spikes downwards, yielding for that particular moment a very small polarization ratio (−20 dB) which deviates greatly, by −15 dB, from the average value (see Figure 16 for the average value).

Having cited examples of so-called "spiking" in our ocean

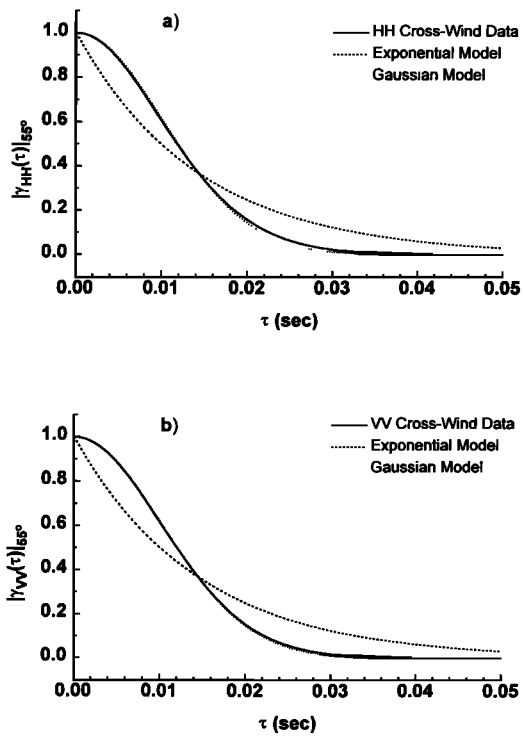

Figure 27. The normalized autocorrelation functions of the horizontal and vertical polarizations versus lag time. Cross-wind look, $\theta_g = 55°$. Here $|\gamma_{HH}|$ and $|\gamma_{VV}|$ are of equal width, and both are wider than the 55° case for upwind look. Both $|\gamma_{HH}|$ and $|\gamma_{VV}|$ are practically Gaussian.

wave data which fall outside the narrow definition of the term, we thus ask: What is spiking? What average decorrelation time between spikes is required? How short should the burst be? How far should the spiking power deviate from some time-averaged value? Lacking a general consensus regarding the definition of a spike or burst, it appears, for the moment, that "spiking" is in the eye of the beholder. *Trizna et al.* [1993] have identified two important mechanisms giving rise to spikes in wave tank experiments. One is a curvature feature caused by extreme steepening of a paddle-generated wave; the other is a steepened blocked wind wave in the trough of the paddle wave. They also express the sentiment that different types of sea spikes should be distinguished and maybe a renaming is in order.

In the narrow sense of the definition of spiking described in the first paragraph in this section, we think that it is simply a hydrodynamically created surface condition which resulted in some nondegenerate object (flotsam, jetsam, waterfowl, flying fish, and seal heads excluded) which favored the horizontal polarization return, yielding HH > VV. In a slightly broader sense, a "burst" is defined as the specular reflection from a very large water surface ($kd \gg 1$) yielding HH = VV. Wave breaking is of course a prime candidate for "horizontal events," sometimes also called "line events," popular for its capability of explaining HH > VV data. There are several constraints, however, on the positive identification of a simple "horizontal" scattering object: (1) the measured polarization ratio defines the possible "aspect ratio" (length/width) of the object, (2) the measured backscattered power defines the effective radar cross section which, taken with point 1, must define a physically realistic shape (for example, a wave-surface area of 0.05 m^2 with dimensions of 2 mm in width and 25 m in length is hydrodynamically unrealistic), and finally, (3) the Doppler frequency provides the information on whether the object is moving at the speed of a fast wave or otherwise. A similar set of constraints exists on the positive identification of a pure specular reflector (for the case HH = VV). Thus, simple models are readily testable for physical reality when invoked to explain scattering sources or objects. We suspect that in general, spiking (in the broad sense) is due to complex shapes and could also be a complicated mixture of several mechanisms. We plan to conduct measurements in upcoming wave tank experiments using ancillary optical diagnostics to record and temporally correlate the scattering objects with the scatterometer signals.

7. Summary

We have performed an ocean experiment of microwave backscattering for a large range of grazing angles (10° to 70°), thereby obtaining grazing angle dependent results. This has enabled us to make the connection between large and small grazing angle backscattering data and thus distinguish between Bragg and faster-than-Bragg components, resulting in a clear identification of different types of scattering sources. With this distinction made, we could elucidate additional features, such as "super" events that are due to the faster-than-Bragg waves and happen not only for small grazing angles, but for all grazing angles. By analyzing time-resolved and wind direction dependent Doppler spectra, we could verify the compelling presence of mechanisms additional to Bragg scattering. We were able to quantify super events and proposed that hydrodynamic processes could occasionally produce nondegenerate, fast scatterers to yield HH equal to or greater than VV. We were also able to see that Bragg scattering is still operative for the horizontal polarization at small grazing angles, albeit overshadowed by the faster-than-Bragg events, so that Rice's theory (or composite model) need not be abandoned too hastily. By examination of the coherence properties of the backscattered signals, we were also able to see that the autocorrelation functions at low grazing angles are clearly distinct for different polariza-

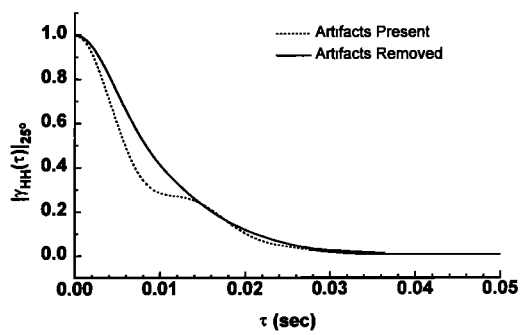

Figure 28. An example of the influence of instrumental artifacts (DC drift and microphonic response at frequencies below ~30 Hz) in the autocorrelation function for a 25° cross-wind case. In this specific case, the data containing the artifacts contribute to a narrowing of the autocorrelation function and the appearance of a "plateau," both of which could be misinterpreted as real effects arising from the scattering surface.

tions, thus providing strong evidence for the presence of lifetime-dominated, non-Bragg-scattering events. Finally, we have found sufficient examples to demonstrate that spiking is in dire need of a clearer definition.

In summary, we believe that our data suggest that there are several mechanisms which contribute to microwave backscattering from ocean waves. The mechanisms may include the following. (1) Bragg scattering, at all angles relative to the wind and at all grazing angles, contributes to the Slow peak in the Doppler spectrum, with polarization ratios in accordance with Rice's theory or composite surface theory (modifications are required, however, at low grazing angles). (2) Scattering from the wave crest vicinity (from microbreaking or macrobreaking events) provides energy at the Fast peak and energy between Fast and Slow peaks (i.e., the "cascade" frequencies) in the Doppler spectrum for upwind look directions at all grazing angles. (3) Preferential diffraction of vertical polarization into the shadow region and multipath scattering represent possible mechanisms to explain the decorrelation of the VV and HH signals (by the former mechanism) and the deviation of the polarization ratio from Rice's theory (by the latter mechanism) at low grazing angles for Slow and Fast signals. (4) Scatterometer returns determined both by the specific orientation of nondegenerate scatterers with respect to microwave fields, and possible multiple (multipath) scattering events which include a reflection at the Brewster angle, can provide the polarization ratio associated with super events.

We find our results to be in good agreement with certain aspects of past ocean experiments, and our present suggestions of scattering mechanisms also echo past conjectures. However, our experiments and synoptic view provide clarification, extensions, and an integration of many past suggestions.

We suggest that the unsolved problem of low-grazing-angle scattering should be approached by formulating a quantitative theory based on the contributions from the proposed scattering features, i.e., Bragg waves, breaking waves, nondegenerate "facets," etc. Of course, not all scattering objects will have to be included in order to account for the predominant backscatter characteristics. The difficulty of incorporating the physics of a breaking wave while retaining Rice's model in a quantitative theory is considerable, and it is easy to understand why currently available theories (e.g., composite theory, higher-order expansions, etc.) are inadequate. However, we hope that the present set of results will provide the necessary experimental evidence to prompt substantial improvements to the present scattering theories.

Appendix A

The effective grazing angle is simply a geometrical correction and is calculated by convolving the R^{-4} range dependence with the measured antenna pattern and the illuminated area (i.e., footprint). The effective grazing angle thus represents the median, since half the return power comes from local grazing angles larger than the median, while the other half comes from local grazing angles smaller than the median. The correction is nonnegligible for small bore sight grazing angles and negligible for large bore sight grazing angles, e.g., the effective angle is 13.1° for a bore sight angle of 10° while the effective angle is 31.5° for a bore sight angle of 30°.

Appendix B

The dielectric constant is computed using $\varepsilon = \varepsilon' - i\varepsilon''$, with real and imaginary parts of the dielectric constant given by

$$\varepsilon' = \frac{\varepsilon_s - \varepsilon_0}{1 + (\omega\tau)^2} + \varepsilon_0 \qquad \varepsilon'' = \frac{\omega\tau}{1 + (\omega\tau)^2}(\varepsilon_s - \varepsilon_0) + \frac{2\sigma_i}{f},$$

where ε_s is the static permittivity, ε_0 is the dielectric constant representing the sum of electronic and atomic polarizations, $\omega = 2\pi f$ is the radial microwave frequency, τ is the characteristic dipole relaxation time of the polar molecule and σ_i, the ionic conductivity, is the additional term to the Debye equation for seawater. For conditions appropriate to experimental sites (temperature of 10°–12°C and salinity of 28–34 international salinity units), we obtain from extant data [*Saxton and Lane*, 1952] $\varepsilon_s = 74$, $\varepsilon_0 = 4.9$, $\tau = 12.2$ ps and $\sigma_i = 0.31 \times 10^{11}$ (electrostatic units).

Appendix C

For a perfect conductor, i.e., for the imaginary part of the dielectric constant tending toward infinity, the polarization ratio becomes a simple expression:

$$\lim_{\varepsilon''\to\infty} \frac{\mathrm{HH}}{\mathrm{VV}} = \left(\frac{\sin^2\theta_g}{1 + \cos^2\theta_g}\right)^2.$$

Appendix D

From our calibration of the antenna pattern, we find the −3-dB beam widths of the horizontal and vertical polarizations are not exactly identical in the azimuthal and vertical planes. This means that the antenna footprint is not exactly identical for the horizontal and vertical polarizations. For example, at 10° grazing angle, the horizontal polarization sees ~18% more surface area in the azimuthal direction while the vertical polarization sees ~35% more area in the range direction. Because of the R^{-4} range dependence of scatterometer signals, the additional contribution to the polarization ratio would be ~1 dB if scatterers were uniformly and isotropically distributed on the surface. Nevertheless, it is a fact that different polarizations will see different areas for real antennas at small grazing angles, which may account for the nonsynchronization of HH and VV signals we observe in our data. Note that the difference in illumination spot size (between polarizations) along the range direction decreases when the grazing angle is increased. The difference in illumination spot size in the azimuthal direction, however, remains independent of the grazing angle.

Appendix E

Microwave scattering from ocean waves is predominantly a diffractive process even if some scattering object has a local surface normal pointed at the scatterometer bore sight. Specular reflection from a "specular facet" occurs when the facet has dimension d such that $kd \gg 1$ (k is the microwave wavenumber). Therefore scattering off a "specular facet" can yield either HH > VV, or HH = VV, or HH < VV, depending on the facet size, shape, and orientation. Thus ray

optics should be used with caution in modeling, since the most interesting effect, that of polarization, is a priori excluded. For the case where specular facets are considered in the context of explaining HH = VV results, see *Kwoh et al.* [1988].

Appendix F

At normal incidence, HH = VV is true only in a time-integrated sense. Furthermore, the additional condition of either a glassy smooth surface or an isotropic distribution of scatterers (waves) is required. Neither condition is realistic for wind wave surfaces, since there are always dominant waves which travel in some preferred direction. The microwave polarization which is aligned with the wave crests will have a different return from the other (orthogonal) polarization. However, at angles approaching normal incidence, scattering from Bragg or faster-than-Bragg waves becomes unresolvable because the Doppler frequency (in the water surface frame) tends to zero as the grazing angle tends to 90°, and only surface elevation motion will be detected. Furthermore, at normal incidence, the Bragg resonance condition has a singularity.

Acknowledgments. This work was conducted under the auspices of Office of Under Secretary of Defense, Naval Warfare and Mobility, under contract with Lawrence Livermore National Laboratory (subcontract B157282). The University of California operates the Lawrence Livermore National Laboratory for the Department of Energy under contract W-7405-ENG-48. The first author is grateful for helpful critiques and generous suggestions provided by W. Plant and three anonymous referees, as well as discussions with D. Holiday, R. Manassee, and B. Werle.

References

Bendat, J. S., and A. G. Piersol, *Random Data: Analysis and Measurement Procedures*, 2nd ed., pp. 252–288, John Wiley, 1986.

Barter, J. D., K. L. Beach, B. M. Lake, P. H. Y. Lee, H. Rungaldier, J. C. Shelton, and R. N. Wagner, Catalog and summary of TRW data from the Joint U.K./U.S. West Coast Experiment, Scotland, 1991, *Rep. 58101-6001-UT-01*, TRW, Redondo Beach, Calif., Sept. 1991.

Barter, J. D., K. L. Beach, and P. H. Y. Lee, Nevis Report: Flow field measurements of a scaled model of Loch Nevis, *Rep. 58101-6003-UT-00*, TRW, Redondo Beach, Calif., Feb. 1992a.

Barter, J. D., et al., Slope gauge data products from Scotland 1991, *Rep. 58101-6001-UT-03*, TRW, Redondo Beach, Calif., April 1992b.

Barter, J. D., et. al., More slope gauge data products from Scotland 1991, *Rep. 58101-6001-UT-04*, TRW, Redondo Beach, Calif., Aug. 1992c.

Barter, J. D., K.L. Beach, C. L. Hindman, B. M. Lake, P. H. Y. Lee, H. Rungaldier, J. C. Shelton, and R. Yee, Calibration of the TRW X-band radar, *Rep. 58101-6001-UT-06*, TRW, Redondo Beach, Calif., Jan. 1993.

Caponi, E., B. M. Lake, P. H. Y. Lee, and H. C. Yuen, A hydrodynamic model for low-grazing-angle backscatter phenomena from the ocean, *Rep. 58101-6002-UT-00*, TRW, Redondo Beach, Calif., Aug. 1993.

Debye, P., Anomalous dispersion for radio frequencies, in *Polar Molecules*, pp. 77–108, Rheinhold, 1929. (Reprinted by Dover, Mineola, N. Y., 1960.)

DeLoor, G. P., and P. Hoogeboom, Radar backscatter measurements from Platform Noordwijk in the North Sea, *IEEE. J. Oceanic Eng., OE-7*, 15–20, 1982.

Duncan, J. R., W. C. Keller, and J. W. Wright, Fetch and wind speed dependence of Doppler spectra, *Radio Sci., 9*, 809–819, 1974.

Ebuchi, N., H. Kawamura, and Y. Toba, Physical processes of microwave backscattering from laboratory wind wave surfaces, *J. Geophys. Res., 98*, 14,669–14,681, 1993.

Goldstein, H., Sea echo, in Propagation of Short Radio Waves, edited by D. E. Kerr, *M.I.T. Radiation Lab. Ser. 13*, pp. 481–527, Mass. Inst. of Technol., Cambridge, 1947. (Reprinted by Dover, Mineola, N. Y., 1965.)

Jessup, A. T., W. C. Keller, and W. K. Melville, Measurements of sea spikes in microwave backscatter at moderate incidence, *J. Geophys. Res., 95*, 9679–9688, 1990.

Jessup, A. T., W. K. Melville, and W. C. Keller, Breaking waves affecting microwave backscatter, 1, Detection and verification, *J. Geophys. Res., 96*, 20,547–20,559, 1991a.

Jessup, A. T., W. K. Melville, and W. C. Keller, Breaking waves affecting microwave backscatter, 2, Dependence on wind and wave condition, *J. Geophys. Res., 96*, 20,561–20,569, 1991b.

Kalmykov, A. I., and V. V. Pustovoytenko, On polarization features of radio signals scattered from the sea surface at small grazing angles, *J. Geophys. Res., 81*, 1960–1964, 1976.

Kerr, D. E., W. T. Fishback, and H. Goldstein, Reflection from the Earth's surface, in Propagation of Short Radio Waves, edited by D. E. Kerr, *M.I.T. Radiation Lab. Ser. 13*, pp. 396–441, Mass. Inst. of Technol., Cambridge, 1947. (Reprinted by Dover, Mineola, N. Y., 1965.)

Kwoh, D. S., and B. M. Lake, A deterministic, coherent, and dual-polarized laboratory study of microwave backscattering from water waves, I, Short gravity waves without wind, *IEEE J. Oceanic Eng., OE-9*, 291–308, 1984.

Kwoh, D. S., B. M. Lake, and H. Rungaldier, Microwave scattering from internal wave modulated surface waves: A shipboard real aperture coherent radar study in the Georgia Strait Experiment, *J. Geophys. Res., 93*, 12,235–12,248, 1988.

Lange, P., and H. Hühnerfuss, Drift response of monolayer slicks to wave and wind action, *J. Phys. Oceanogr., 8*, 142–150, 1978.

Lee, P. H. Y., Microwave studies of surface wave–internal wave interactions, *Rep. 26063-6010-RU-00*, TRW, Redondo Beach, Calif., July 1976.

Lee, P. H. Y., Doppler measurements of the effects of gravity waves on wind-generated ripples, *J. Fluid Mech., 81*, 225–240, 1977.

Lee, P. H. Y., et al., Recent advances in ocean surface characterization by a scanning laser slope gauge, *Proc. SPIE Int. Soc. Photogramm. Eng., 1749*, 234–243, 1992.

Leykin, A. I., I. Ye. Ostrovskiy, A. D. Rozenberg, V. G. Ruskevich, and I. M. Fuks, The effect of long waves on energy spectra of radar signals scattered from a sea surface, *Izv. Vyssh. Ucheb. Zaved. Radiofiz., 3*, 346–357, 1975.

Long, M. W., On a two-scatter theory of sea echo, *IEEE Trans. Antennas Propag., AP-22*, 667–672, 1974.

Lyzenga, D. R., A. L. Maffett, and R. A. Shuchman, The contribution of wedge scattering to the radar cross section of the ocean surface, *IEEE Trans. Geosci. Remote Sens., GE-21*, 502–505, 1983.

Mel'nichuk, Yu. V., and A. A. Chernikov, Spectra of radar signals from sea surfaces for different polarizations, *Izv. Acad. Sci. USSR Atmos. Oceanic Phys.*, Engl. transl., *7*, 17–24, 1971.

Miller, S. J., O. H. Shemdin, and M. S. Longuet-Higgins, Laboratory measurements of modulation of short-wave slopes by long surface waves, *J. Fluid Mech., 233*, 389–404, 1991.

Peake, W. H., Theory of radar return from terrain, *IRE Natl. Conv. Rec., 7*(1), 21–39, 1959.

Pidgeon, V. W., Doppler dependence of radar sea return, *J. Geophys. Res., 73*, 1333–1341, 1968.

Plant, W. J., Bragg scattering of electromagnetic waves from the air/sea interface, in *Surface Waves and Fluxes*, vol. II, edited by G. L. Geernaert and W. J. Plant, pp. 41–108, Kluwer Academic, Hingham, Mass., 1990.

Rice, S. O., Reflection of electromagnetic waves from slightly rough surfaces, *Commun. Pure Appl. Math., 4*, 351–378, 1951.

Saxton, J. A., Electrical properties of water: Reflection characteristics of water surfaces of V.H.F., *Wireless Eng., 26*, 288–292, 1949.

Saxton, J. A., and J. A. Lane, Electrical properties of sea water, *Wireless Eng., 29*, 269–275, 1952.

Trizna, D. B., J. P. Hansen, P. Hwang, and J. Wu, Laboratory studies of radar sea spikes at low grazing angles, *J. Geophys. Res., 96*, 12,529–12,248, 1991.

Trizna, D. B., J. P. Hansen, P. Hwang, and J. Wu, Ultra-wideband radar studies of steep crested waves with scanning laser measurements of wave slope profiles, *Dyn. Atmos. Oceans*, *20*, 33–53, 1993.

Valenzuela, G. R., Scattering of electromagnetic waves from the ocean, in *Surveillance of Environmental Pollution and Resources by Electromagnetic Waves*, edited by T. Lund, pp. 196–226, D. Reidel, Norwell, Mass., 1978.

Valenzuela, G. R., and M. B. Laing, Study of Doppler spectra of radar sea echo, *J. Geophys. Res.*, *75*, 551–563, 1970.

Ward, K., C. J. Baker, and S. Watts, Maritime surveillance radar, 1, Radar scattering from the ocean surface, *IEE Proc.*, *137*, 51–62, 1990.

Wetzel, L. B., A model for sea backscatter intermittency at extreme grazing angles, *Radio Sci.*, *12*, 749–756, 1977.

Wetzel, L. B., On microwave scattering by breaking waves, in *Wave Dynamics and Radio Probing of the Ocean Surface*, edited by O. M. Phillips and K. Hasselmann, pp. 273–284, Plenum, New York, 1986.

Wright, J. W., A new model for sea clutter, *IEEE Trans. Antennas Propag.*, *AP-16*, 217–223, 1968.

J. D. Barter, K. L. Beach, C. L. Hindman, B. M. Lake, P. H. Y. Lee, H. Rungaldier, J. C. Shelton, A. B. Williams, R. Yee, and H. C. Yuen, TRW Space and Electronics, R1-1008, One Space Park, Redondo Beach, CA 90278.

(Received January 28, 1994; revised October 19, 1994; accepted October 19, 1994.)